PD-L1-Binding Antigen Presenters: Redirecting Vaccine-Induced Antibodies for Tumor-Agnostic Immunotherapy

Huixin Gao[1], *Lijuan Lu*[2], *Xiaoxiao Xiong*[3], *Yi Li*[3], *Donghui Hu*[4], *Duo Zhang*[3], *Zhiwei Feng*[3], *Cong Liu*[3], *Nannan Liu*[3], *Xiaoli Li*[3], *Jizhou Tan*[5], *Ting Liu*[6], *Ling Peng*[7], *Lu Lu*[7], *Huiyi Feng*[8], *Yan Zhong*[9], *Guisen Tan*[10], *Zhicheng Zhang*[11], *Liqin Huang*[12], *Chao Su*[13], *Ying Xue*[3]*, *Shuo Song*[14]*, *Wenxia Fan*[3]*, *Wei Wang*[15]*, *Fan Zou*[3]*

[1]Department of Clinical Laboratory, Guangzhou Women and Children Medical Center, Guangzhou Medical University, Guangzhou, Guangdong 510600, P.R. China.

[2]Department of Medical Oncology, the Third Affiliated Hospital of Sun Yat-sen University, Guangzhou, Guangdong 510665, P. R. China.

[3]Faculty of Pharmaceutical Sciences, Shenzhen University of Advanced Technology, Shenzhen, Guangdong 518107, P.R. China.

[4]Department of Traditional Chinese Medicine, The Third People's Hospital of Hubei Province, Wuhan, Hubei 430033, P.R. China

[5]The First Affiliated Hospital, Sun Yat-sen University, Guangzhou 510080, P.R. China.

[6]The Second Clinical Medical College, Guangzhou University of Chinese Medicine, Clinical Laboratory/State Key Laboratory of Traditional Chinese Medicine Syndrome, Guangdong Provincial Hospital of Chinese Medicine, Guangzhou 510120, P.R. China.

[7]Beijing Luzhu Biotechnology Co. Ltd., Beijing 101149, P.R. China.

[8]Department of Oncology, Shenzhen Hospital of Southern Medical University, Shenzhen, Guangdong 518110, P.R. China.

[9]Department of Pathology, Shenzhen Hospital of Southern Medical University, Shenzhen, Guangdong 518110, P.R. China.

[10]The First Affiliated Hospital of Guilin Medical University, Guilin, Guangxi 541001, P.R. China.

[11]Zhongshan Institute for Drug Discovery, Zhongshan, Guangdong 528451, P.R. China.

[12]Shenzhen Blood Center, Shenzhen, Guangdong 518035, P.R. China.

[13]Jilin Province Jilin Hospital of Integrated Traditional Chinese and Western Medicine, Jilin, Jilin 132000, P.R. China.

[14]Faculty of Life and Health Sciences, Shenzhen University of Advanced Technology, Shenzhen, Guangdong 518107, P.R. China.

[15]Department of Thoracic Surgery, the Second Affiliated Hospital of Guangzhou Medical University, Guangzhou, Guangdong 510260, P.R. China.

H.X.G., L.J.L., X.X.X., Y. L., and D.H.H. contributed equally to this work.

*Correspondence: xueying@suat-sz.edu.cn; songshuo@suat-sz.edu.cn; fanwenxia@suat-sz.edu.cn; 2011682026@gzhmu.edu.cn; zoufan@suat-sz.edu.cn

ABSTRACT

The efficacy of immunotherapy in enhancing antitumor immunity in solid tumors remains limited, primarily due to the insufficient immunogenicity of tumor cells. In contrast, vaccination and natural viral infections can generate durable, high-titer antiviral antibodies. A modular Programmed Death-Ligand 1 (PD-L1)-binding antigen presenter (PBAP-gE) has been engineered to tether varicella-zoster virus glycoprotein E (gE) to PD-L1 expressed on tumor cell surfaces. This innovative construct leverages pre-existing anti-gE antibodies to trigger antibody-dependent effector mechanisms. PBAP-gE effectively bound to PD-L1-positive tumor cells and, together with vaccine-induced anti-gE antibodies, potentiated NK cell-mediated antibody-dependent cellular cytotoxicity (ADCC) *in vitro* and induced significant tumor regression in murine models. The PBAP platform is modular and versatile. For example, a PBAP-Her2 construct synergized with Trastuzumab and Kadcyla to kill Human Epidermal growth factor Receptor 2 (HER2)-negative, PD-L1-positive cells. This strategy represents an innovative strategy for enhancing PD-L1-targeted therapies by leveraging pre-existing antibodies induced by viral infections or vaccines, alongside commercially available antibody-based therapies.

Keywords：

PD-L1-binding antigen presenter (PBAP); Tumor-agnostic immunotherapy; Vaccine-induced antibodies; Antibody-dependent cellular cytotoxicity (ADCC); Antibody drug conjugates (ADC)

1. Introduction

Recent advances in high-throughput technologies, particularly single-cell sequencing, spatial transcriptomics, and multiplex immunohistochemistry, have significantly deepened our understanding of the tumor microenvironment (TME), offering a more nuanced view of how tumors evade immune surveillance.[1-3] Despite the infiltration of various immune cell populations, such as cytotoxic T lymphocytes (CTLs) and natural killer (NK) cells, the ability of these cells to effectively recognize and eliminate tumor cells is often hindered. This failure is primarily due to immune evasion mechanisms, such as antigen loss, defects in antigen presentation, and the establishment of an immunosuppressive TME.[3,4] Notably, viral antigen-specific bystander T cells within the TME remain functional but cannot effectively target tumor cells due to the lack of tumor-specific antigens.[5-14] This highlights a critical gap in the immune response, where the presence of functional immune cells is insufficient to overcome the tumor's immune evasion strategies.

To address these issues, innovative therapeutic approaches, including the use of oncolytic viruses (OVs) and engineered bacteria, have emerged as promising platforms for personalized cancer vaccines. These strategies aim to enhance immune recognition by "tagging" tumor cells with exogenous antigens. For example, OVs engineered to carry the ovalbumin (OVA) antigen, in combination with OVA T-cell receptor-1 (OT-1) T cells or OT-1 peptide vaccines, have demonstrated synergistic tumor-killing effects in preclinical mouse models.[15] Beyond Major Histocompatibility Complex (MHC)-peptide complex presentation, OVs can also deliver large exogenous proteins on tumor cell surfaces. For example, OVs based on Newcastle disease virus (NDV) have been modified to express porcine α1,3-galactosyltransferase (α1,3GT) on the surfaces of infected tumor cells. This modification triggers hyperacute rejection

through pre-existing anti-αGal antibodies, thereby leading to ~~the~~ effective elimination of tumors.[16]

Similarly, a novel dual-virus strategy has been developed, engineering OVs to express truncated HER2 antigens on the surface of tumor cells. This innovative approach enables the use of Her2-targeted antibody-drug conjugates (ADCs, such as Kadcyla) even in cancers that are HER2 negative, effectively overcoming the limitations posed by the absence of HER2 antigens.[17] Additionally, engineered bacteria delivering non-tumor neoantigens have also shown promise in training the immune system to target and destroy cancer cells presenting identical antigens.[18] Remarkably, a significant proportion of bystander T cells have been observed to recognize virus-related antigens rather than tumor-specific antigens within the TME. These bystander T cells play a crucial role in shaping the TME and influencing antitumor immune responses.[5-14] Studies have demonstrated that viral-specific T cells, induced by Lymphocytic Choriomeningitis Virus (LCMV) infection or Severe Acute Respiratory Syndrome Coronavirus 2 (SARS-CoV-2) vaccination, can function as bystander T cells within the TME of tumor-engrafted mice, and OVs engineered to express relevant viral peptides effectively "tag" the tumors with these viral antigens, thereby repurposing the viral-specific T cells to target and eliminate the tumors in the engrafted mice.[19] These findings motivate a tumor-agnostic strategy: present an immunogenic, non-tumor antigen on tumor surfaces to recruit pre-existing humoral effectors and bypass antigen-loss mediated evasion.

PD-L1 is abundantly expressed on tumor cells, tumor-suppressive cells and antigen-presenting cells, making it a key target for immunotherapy.[20,21] Therapeutic agents targeting PD-L1, including monoclonal antibodies and ADCs, not only function through immune checkpoint blockade, which relieves inhibition of T cells,

but also directly kill tumor cells via antibody-dependent cellular cytotoxicity (ADCC) and the targeted delivery of cytotoxic agents by ADCs.[22-26] Nevertheless, the objective response rates achieved by PD - L1 blockade monotherapy in solid tumors are still relatively low, highlighting the urgent need for more effective therapeutic strategies.[27,28] Thus, the development of PD-L1-targeted therapies, such as ADCs and bispecific antibodies, has gained increasing attention.[22,29,30] Several PD-L1 ADCs, including SGN-PDL1V (PF-08046054), HLX43 (EOC Pharma), and DB-1419 (DualityBio), are currently in clinical trials, offering the potential to broaden treatment options.[31-34]

Building upon the promising "tagging tumor cells with viral antigen peptides" strategy, which has demonstrated the potential to repurpose bystander T cells for tumor eradication[19], we propose an innovative approach to enhance tumor-targeted immune responses. This strategy leverages the long-term stability of antibodies induced by viral infections or vaccines, including those against pathogens such as measles virus, mumps virus, rubella virus, varicella-zoster virus (VZV), Epstein-Barr virus (EBV), Clostridium tetani (tetanus-causing bacterium), and Corynebacterium diphtheriae (diphtheria-causing bacterium). Notably, these antibodies remain detectable for decades, even in cancer patients.[35-41] In previous experiments, we introduced the recombinant zoster protein vaccine LZ901 (Beijing Luzhu Biotechnology Co., Ltd.), which has been confirmed to exhibit robust immunogenicity in both mice and humans.[42,43] In tumor-bearing C57BL/6 mice immunized with LZ901, we observed enrichment of B cells within tumor tissues. Notably, tumor-infiltrating B cells produced significantly higher levels of anti-gE IgG antibodies than B cells isolated from the spleen (Fig. S1).

Drawing from these findings, we describe a modular platform termed PD-L1 binding antigen presenter (PBAP), designed to tether viral antigen to tumor cells through PD-L1 binding. As a proof of concept, we engineered PBAP-gE by fusing the extracellular domain of PD-1 (soluble PD - 1, sPD-1) to gE of VZV and included an Fc domain to boost stability. This design leverages two key principles: (i) PD-L1 is broadly expressed across diverse tumor types, and (ii) varicella vaccination elicits durable anti-gE antibody responses in most adults. Critically, this enables antibodies, whether induced by vaccination or natural VZV infection, to specifically target tumor cells and redirect the immune response against them (Scheme 1).

2. Results

2.1 PBAP-gE Combined with Vaccine-Induced Endogenous Antibodies Exhibits Anti-Tumor Activity *In Vitro*

The PBAP-gE fusion protein was constructed by fusing the extracellular domain of murine PD-1 (sPD-1) to gE using a flexible linker. An Fc domain was included at the C-terminus of the construct to prolong its circulation half-life in the bloodstream and to enhance its stability and efficacy (Fig. 1A, Fig. S2A, B). Structural modeling of PBAP-gE using AlphaFold 3 revealed no significant steric hindrance between the sPD-1 domain and the gE domain (Fig. 1B). PBAP-gE could be stably detected in mice over 72 hours; in contrast, the stable existence time of sPD-1-gE in mice is significantly shortened, being only 8 hours (Fig. 1C).

To validate that PBAP-gE competitively blocks the binding of PD-L1 to PD-L1 antibodies *in vitro*, recombinant PD-L1 protein and 4T1 cells engineered to stably overexpress murine PD-L1 (designated 4T1-PD-L1-OE) via lentiviral transduction and subsequent enrichment were employed. The results of ELISA and flow cytometer

analysis confirmed that PBAP-gE effectively inhibited the interaction of PD-L1 antibodies with both soluble PD-L1 protein and cell surface PD-L1 (Fig. 1D, E).

To produce serum enriched with gE-specific antibodies for subsequent *in vitro* experimental use, C57BL/6 mice were immunized with the recombinant zoster protein vaccine (LZ901, Beijing Luzhu Biotechnology Co., Ltd.) on days 0 and 21, at a dose of 5 μg per mouse. On Day 28, serum samples were collected via retro-orbital bleeding for subsequent assays. The *in vitro* anti-tumor activity of the PBAP-gE construct in combination with vaccine-induced antibodies was initially evaluated using a lactate dehydrogenase (LDH) release assay. Murine KIL C.2 cells (an NK cell line) were co-incubated with PBAP-gE and serum from LZ901-immunized mice. The ability of these cells to lyse 4T1-PD-L1-OE tumor cells was then assessed. KIL C.2 cells, co-incubated with PBAP-gE and serum from LZ901-immunized mice, exhibited significantly enhanced cytotoxicity against 4T1-PD-L1-OE tumor cells (Fig.1F, left panel). Control groups, including KIL C.2 cells alone, KIL C.2 cells treated with gE protein and serum from LZ901-immunized mice, or KIL C.2 cells treated with PBAP-gE and serum from saline-immunized mice, exhibited negligible cytotoxicity. These findings underscore the essential role of PBAP-gE in concert with vaccine-induced antibodies in augmenting NK cell - mediated immune responses.

To further confirm the specificity of NK cell-mediated cytotoxicity via PBAP-gE, CRISPR - Cas9 was employed to generate a PD-L1 knockout variant of the 4T1 cell line (designated 4T1-PD-L1-KO). After PD-L1 knockout in 4T1 cells (4T1-PD-L1-KO), PBAP-gE and vaccine serum failed to enhance KIL C.2-mediated killing of 4T1-PD-L1-KO cells (Fig.1F, right panel), highlighting the essential role of PD-L1 expression on tumor cells for PBAP-mediated immune engagement.

This result underscores the necessity of PD-L1 recognition in the mechanism of action of PBAP-gE, which facilitates immune targeting and tumor eradication through the recruitment of viral-specific antibodies. The functional activation of KIL C.2 cells was further analyzed, Specifically, the production of IFN-γ and the expression of inhibitory receptors in KIL C.2 cells, which were previously assessed in the cytotoxicity assay, were evaluated using flow cytometer. Compared to control groups, KIL C.2 cells in the experimental group exhibited significantly higher levels of IFN-γ expression, which is a hallmark of NK cell activation. Additionally, the experimental group also demonstrated a significant increase in the proportion of NKG2A-negative KIL C.2 cells (Fig. 1G, Fig. S3), indicating reduced inhibition and enhanced activation of KIL C.2 cells. This suggests that the combination of PBAP-gE and vaccine-induced antibodies not only enhances KIL C.2 cell-mediated tumor lysis but also reprograms KIL C.2 cells toward a more potent and less inhibited effector phenotype.

2.2 PBAP-gE Delivered via Chimeric Antigen Receptor T-Cells （CAR-T Cells) and Intratumoral Injection Exhibits Anti-Tumor Activity in Murine Tumor Models

In our previous research, A range of CAR - T cells were engineered utilizing strategies including the knockout of inhibitory receptors, the overexpression of functional proteins, and the implementation of combination therapies. achieving effective clearance of virus-infected cells and solid tumors in both animal models and clinical trials.[44-49] In contrast to complex oncolytic virus (OV) systems, we propose utilizing chimeric antigen receptor T (CAR-T) cells to selectively deliver PBAP to tumor sites, ensuring that PBAP expression is activated only upon CAR-T cell activation. This approach not only minimizes off-target effects but also mitigates the

risk of PBAP-gE being neutralized by vaccine-induced antibodies in the bloodstream. Furthermore, this “living drug” delivery system could establish immunological memory, enabling CAR-T cells to patrol and surveil tumor cells for extended periods. To this end, a multicistronic expression system was developed. In this system, the CAR gene, which includes an anti-CD19 single-chain variable fragment (scFv) used as a control and an anti-Trop2 scFv, was designed for sustained expression. Meanwhile, the PBAP-gE expression was controlled by an NFAT promoter, ensuring that PBAP-gE expression is restricted to conditions of CAR-T cell activation (Fig. 2A). Although CAR-T cells have been integrated with various treatment modalities, including chemotherapy, radiotherapy, and immune checkpoint inhibitors (ICIs), their combination with NK cells remains largely unexplored. In the current study, we conceptualized a novel approach that integrates CAR-T and NK cells via secreted PBAP "tagging" synergized with vaccine-induced antibodies, aiming to leverage both CAR-T and NK cells in a combined therapeutic strategy (Fig. 2B).

To evaluate the effectiveness of Trop2-CAR-T cells (Trop2-CAR) and Trop2-CAR-T cells expressing PBAP-gE (Trop2-CAR-PBAP) *in vitro*, the properties and functions of these cells, including cytotoxicity and PBAP-gE secretion, were assessed. Trop2-CAR-PBAP cells exhibited a slight yet nonsignificant decrease in retroviral transduction efficiency (transduction rate) and CAR expression (mean fluorescence intensity, MFI), likely due to the inclusion of additional PBAP cistrons (Fig. S4A). B16 cells engineered to overexpress Trop2 (B16-Trop2), which can stably express the Trop2 protein, can be used to evaluate the cytotoxic effects of CAR-T cells against Trop2-positive tumors. Notably, both Trop2-CAR and Trop2-CAR-PBAP demonstrated comparable cytotoxicity against B16-Trop2 cells, indicating that the minor reduction in CAR expression did not compromise their ability to lyse target

243 cells (Fig. S4B). Furthermore, Trop2-CAR-PBAP cells secreted minimal PBAP when
244 co-cultured with B16-F10 cells (a murine melanoma cell line, as a negative control),
245 likely driven by cytokines secretion from the CAR-T cells themselves upon activation.
246 However, when cocultured with B16-Trop2 cells, the concentration of secreted PBAP
247 was significantly elevated, highlighting the specific activation of Trop2-CAR-PBAP
248 cells by Trop2-expressing target cells (Fig. S4C).

249 Next, the dual-targeting combination strategy was tested in syngeneic tumor models.
250 B16-Trop2 cells were injected intratumorally into 6-8 week-old male C57BL/6 mice.
251 Experimental groups included Trop2-CAR-T cells expressing PBAP-gE
252 (Trop2-CAR-PBAP), control groups with CD19-CAR-T cells (CD19-CAR), and
253 non-PBAP-expressing Trop2-CAR-T cells (Trop2-CAR). Additionally, the effect of
254 different PBAP-gE administration routes was evaluated by combining Trop2-CAR-T
255 cells with PBAP-gE delivered intravenously (*i.v.*), intraperitoneally (*i.p.*), or
256 intratumorally *(i.t.*), creating three experimental groups: Trop2-CAR + PBAP (*i.v.*),
257 Trop2-CAR + PBAP (*i.p.*), and Trop2-CAR + PBAP (*i.t.*). All CAR-T cell infusions
258 were administered intravenously. Mice were immunized with the recombinant zoster
259 vaccine LZ901 on Days 0 and 21 (5 μg/mouse/dose), and serum was collected on Day
260 27. On Day 28, mice were subcutaneously injected with B16-Trop2 cells. When
261 average tumor volumes reached approximately 100 mm^3 (Day 35), treatments were
262 initiated as per the experimental protocol, which included intravenous infusion of
263 various CAR-T cells (1×10^6) and concurrent administration of PBAP-gE via *i.v.*, *i.p.*,
264 or *i.t.* routes. Tumor growth was monitored until Day 42, at which point mice were
265 euthanized for collection of serum and tumor tissues (Fig. 2C). Results demonstrated
266 that the Trop2-CAR-PBAP group and the Trop2-CAR + PBAP (*i.t.*) group exhibited
267 significant tumor control and regression. In contrast, intravenous and intraperitoneal

PBAP-gE administration resulted in only modest anti-tumor effects (Fig. 2D, E). This indicates that PBAP may be vulnerable to interference from endogenous antibodies, which could potentially undermine its anti-tumor efficacy. In contrast, CAR-T cells seem to serve as a more effective delivery vehicle for PBAP-gE, thereby enhancing its therapeutic potential. Further analysis of tumor-infiltrating immune cells revealed that while CAR-T cell infiltration did not differ significantly across groups, the number of CAR-T cells was notably lower in the Trop2-CAR-PBAP treatment group compared to the Trop2-CAR group. However, the frequencies of B cells and NK cells were significantly elevated in both the Trop2-CAR-PBAP and Trop2-CAR + PBAP (*i.t.*) groups (Fig. 2F, Fig. S5). Moreover, tumor burden inversely correlated with gE-specific IgG antibody levels in these groups, suggesting that ADCC mediated by vaccine-induced antibodies and NK cells played a key role in anti-tumor efficacy (Fig. 2G, H, Fig. S6). In conclusion, the integration of CAR-T and NK cells through secreted PBAP, synergized with vaccine-induced antibodies, demonstrated superior anti-tumor efficacy both *in vitro* and *in vivo*.

2.3 Endogenous Vaccine-Induced Antibodies, Rather than Virus-Specific T Cells, Are the Primary Effectors in PBAP-gE–Mediated Tumor Suppression

LZ901 have previously been shown to elicit both robust humoral and cellular immune responses, including the generation of high titers of anti-gE antibodies, as well as strong $CD4^+$ and $CD8^+$ T-cell responses. These immune responses are crucial for protection against VZV infection, with T-cell immunity potentially playing a key role.[42,43] Given the potential of PBAP-gE to be processed and presented by antigen-presenting cells (APCs) via major histocompatibility complex (MHC) class I pathways, which could activate gE-specific cytotoxic $CD8^+$ T cells, we sought to evaluate the contributions of antibodies versus $CD8^+$ T cells to the anti-tumor efficacy

of PBAP-gE. Moreover, tumor cells may also internalize and process PBAP-gE directly, adding complexity to the interplay between immune effectors and tumor cells.

To address these questions, mice were immunized with the recombinant zoster vaccine LZ901 on Days 0 and 21 to generate vaccine-induced immune responses. On Day 28, mice were subcutaneously inoculated with B16-fLuc cells, a murine melanoma cell line engineered to express firefly luciferase. To selectively deplete B cells or $CD8^+$ T cells, mice were treated with specific blocking antibodies. B cell depletion was achieved through intraperitoneal injection of anti-CD19 (clone 1D3), anti-CD22 (clone CY34.1), and anti-B220 (clone RA3-6B2) antibodies (150 μg of each antibody per mouse) on Day 33, targeting the B cell lineage at multiple stages of development. For $CD8^+$ T cell depletion, an anti-CD8 antibody (clone 16-0081-85, 150 μg/mouse) was administered similarly. On Day 35, mice were given intratumoral injections of PBAP-gE (150 μg/mouse), and tumor growth was monitored using an *in vivo* imaging system (IVIS), allowing for real-time tracking of tumor size and dynamics (Fig. 3A). Results showed that B cell depletion significantly impaired the anti-tumor efficacy of PBAP-gE, whereas $CD8^+$ T cell depletion had minimal effect (Fig. 3B). These findings strongly suggest that the primary mechanism by which PBAP-gE mediates tumor suppression is through the action of vaccine-induced antibodies, rather than through the activation of gE-specific $CD8^+$ T cells.

2.4 Anti-Tumor Efficacy Strongly Correlates with Levels of Vaccine-Induced Endogenous Antibodies

In our previous research, we developed a series of nanoparticle-based vaccines against SARS-CoV-2, which demonstrated significantly enhanced immunogenicity, eliciting potent and durable immune responses.[50-53] To further investigate the relationship

between the levels of endogenous antibodies and the therapeutic efficacy of PBAP-based treatments, we assessed the anti-tumor effects of PBAP-gE in conjunction with vaccines of varying immunogenicity. Specifically, we compared gE-specific antibody responses and subsequent anti-tumor outcomes following immunization with three distinct vaccine platforms: (i) a low-immunogenicity gE subunit vaccine, (ii) the LZ901 recombinant zoster vaccine, and (iii) a high-immunogenicity nanoparticle-based GE-I53-50 virus-like particle (VLP) vaccine, which is self-assembled from I53-50B and GE-I53-50A (Fig. 4A, B, Fig. S7A).[54] This approach allowed us to systematically evaluate how different levels of vaccine-induced immunity influence the efficacy of PBAP-gE in a tumor model, providing valuable insights into the interplay between immunogenicity and therapeutic outcomes.

Mice were randomly assigned to six experimental groups (n = 8 per group): saline control, GE subunit vaccine, LZ901 vaccine, GE-I53-50 VLP vaccine, and two GE-I53-50 VLP vaccine with antibody blocking groups (one with B cell depletion and one with $CD8^+$ T cell depletion). Vaccinations were administered on Days 0 and 21 (5 μg/mouse/dose), and serum were collected on Day 27. On Day 28, tumors were established via subcutaneous injection of B16-Trop2 cells. To assess the contributions of humoral and cellular immunity, B cell and $CD8^+$ T cell depletions were performed on Day 33. On Day 35, PBAP-gE was administered intratumorally (150 μg/mouse) as part of the treatment regimen (Fig. 4C).

Our results revealed that the GE-I53-50 VLP vaccine elicited the most robust anti-tumor response, exhibiting therapeutic efficacy comparable to that of the LZ901 vaccine. Mice vaccinated with the GE-I53-50 VLP vaccine exhibited markedly diminished tumor growth, underscoring the substantial influence of highly

immunogenic vaccines on enhancing anti-tumor immunity (Fig. 4D, E). Importantly, B cell depletion markedly diminished the therapeutic efficacy of PBAP-gE, while $CD8^+$ T cell depletion did not result in a significant change in tumor control, further emphasizing the crucial role of humoral immunity, particularly vaccine-induced antibodies, in mediating the anti-tumor effects of PBAP-gE.

To elucidate the mechanisms underlying the anti-tumor effects observed with the GE-I53-50 VLP vaccine and to compare its efficacy with other vaccines, a comprehensive analysis of immune cell infiltration and antibody responses were detected. Immunophenotyping analysis revealed no significant differences in $CD4^+$ or $CD8^+$ T cell infiltration among the experimental groups, suggesting that the anti-tumor efficacy was not primarily driven by CAR-T cell-mediated cytotoxicity (Fig. S7B, C). In contrast, NK cell frequencies were notably elevated in both tumor and spleen tissues of mice that were immunized with either the LZ901 or GE-I53-50 VLP vaccines (Fig. 4F). These results suggest that NK cells, in conjunction with vaccine-induced antibodies, play a crucial role in enhancing the immune-mediated clearance of tumor cells. Moreover, serum gE-specific IgG levels at the experimental endpoint were inversely correlated with tumor volume, providing compelling evidence that higher titers of vaccine-induced antibodies contribute to enhanced anti-tumor effects. This correlation further underscores the critical role of antibody-dependent mechanisms, such as ADCC, in facilitating tumor eradication in this therapeutic context (Fig. 5A-C, Fig. S7D).

Taken together, our findings demonstrate that PBAP-gE, when synergized with vaccine-induced antibodies, significantly enhances anti-tumor immune responses. Humoral immunity, particularly the levels of gE - specific antibodies, plays a central role in the observed therapeutic efficacy. These results highlight the potential of

combining PBAP-based therapies with high-immunogenicity vaccines to achieve robust, sustained anti-tumor immunity.

2.5 PBAP Designed with Tumor-Specific Antigens Enable *In Vitro* Anti-Tumor Activity in Combination with Commercial Antibodies and ADCs

To further assess the anti-tumor efficacy of the "tagging strategy" with PBAP and its potential for synergistic effects with approved antibody therapies, we engineered a Her2-targeted PBAP (PBAP-Her2) by fusing the extracellular domain of human PD-1 (sPD-1) with Domain *IV* of the Her2 protein via a flexible linker, followed by the addition of an Fc region to enhance protein stability and extend its half-life (Fig. 6A, Fig. S8). Structural modeling of PBAP-Her2 using AlphaFold 3 revealed no significant steric hindrance between the sPD-1 domain and the Domain *IV* of the Her2 (Fig. 6B). PBAP-Her could be stably detected in mice over 120 hours; in contrast, the stable existence time of sPD-1-Her2 in mice is significantly shortened, being only 4 hours (Fig. 6C). *In vitro* experimental verification has demonstrated that PBAP-Her2 inhibits the binding of PD-L1 protein to PD-L1 antibodies. Additionally, it blocks the interaction between PD-L1 expressed on MDA-MB-231-PD-L1-OE cells and PD-L1 antibodies (Fig. 6D, E).

This dual-functional construct is designed to engage PD-L1 on tumor cells via the sPD-1 domain, while concurrently being recognized by Her2-targeting monoclonal antibody Trastuzumab (Herceptin) and the antibody-drug conjugate Kadcyla (T-DM1), which combines Trastuzumab with a potent cytotoxic agent. The human-derived MDA-MB-231-PD-L1-OE tumor model, a Her2-negative breast cancer cell line engineered to stably overexpress human PD-L1 via lentiviral transduction and subsequent enrichment, were introduced to explore the potential synergistic effects with Trastuzumab and Kadcyla (Fig. 6F).

To assess the potential of PBAP in synergy with Trastuzumab for mediating antibody-dependent cellular cytotoxicity (ADCC) and antibody-dependent cellular phagocytosis (ADCP), we employed two distinct reporter assays using Jurkat-FcγRIIIa and Jurkat-FcγRIIa cells, each expressing their respective Fc receptors and an NFAT-driven luciferase reporter. In these assays, PBAP-Her2 in combination with Trastuzumab generated robust ADCC signals, alongside moderate ADCP activity, in Her2-negative MDA-MB-231-PD-L1-OE cells (Fig. 6G). Importantly, further LDH release assays demonstrated that NK cells, when combined with PBAP-Her2 and Trastuzumab, effectively mediated ADCC and facilitated killing of MDA-MB-231-PD-L1-OE cells, as evidenced by a significant increase in cytotoxicity compared to control groups (Fig. 6H, left panel). These results highlight the synergistic action of PBAP-Her2 and Trastuzumab in promoting NK cell-mediated tumor cell elimination.

To confirm the essential role of PD-L1 in the observed cytotoxic effects, we generated a PD-L1 knockout variant of the MDA-MB-231 cell line using CRISPR (designated MDA-MB-231-PD-L1-KO). In this PD-L1-deficient cells model, the cytotoxicity mediated by PBAP-Her2 and Herceptin was reduced to levels comparable to the control group, further validating the critical involvement of PD-L1 in the immune engagement process (Fig. 6H, right panel). flow cytometer analysis revealed a marked increase in IFN-γ production by NK cells and a reduction in the proportion of $NKG2A^+$ NK cells in the experimental group, suggesting enhanced activation and diminished inhibition in response to PBAP-Her2 + Herceptin treatment (Fig. 6I, Fig. S9).

Finally, to further investigate the potential synergistic effect of PBAP-Her2 with ADCs, we evaluated the combinatorial cytotoxicity of PBAP-Her2 in combination

418 with Kadcyla, using Adcetris (a CD30-targeting ADC) as a negative control. The
419 inclusion of PBAP-Her2 significantly enhanced the cytotoxic activity of Kadcyla
420 against MDA-MB-231-PD-L1-OE cells were observed by WST-8 viability assay, as
421 evidenced by a marked reduction in cell viability compared to either treatment alone
422 (Fig. 6J). This suggests that PBAP-Her2 enhances the therapeutic efficacy of
423 HER2-targeted ADCs, offering a novel strategy to improve treatment outcomes in
424 HER2-negative tumors.

425 Collectively, these results highlight the potential of the PBAP-Her2 strategy, in
426 combination with Trastuzumab and NK cells or Kadcyla, to effectively target and
427 eliminate HER2-negative tumor cells. By harnessing both immune and
428 antibody-dependent mechanisms, this approach not only boosts immune cell-mediated
429 cytotoxicity but also holds great promise for enhancing the efficacy of ADC-based
430 therapies in solid tumors.

431 **2.6 PBAP-Her2 Combined with ADCs Demonstrates *In Vivo* Efficacy in NSG**
432 **Tumor-Bearing Mice**

433 To evaluate the *in vivo* therapeutic efficacy, we established a subcutaneous
434 MDA-MB-231 tumor model in NSG mice. Tumors were induced by subcutaneous
435 injection of MDA-MB-231 cells. Once the tumors reached an approximate volume of
436 100 mm^3, the mice were randomly assigned to four experimental groups (n = 5 per
437 group): PBAP-Her2 alone (control), Kadcyla alone (control), PBAP-Her2 + Adcetris
438 (a CD30-targeting ADC, control), and PBAP-Her2 + Kadcyla, and treatment
439 regimens were initiated.

440 The therapeutic protocol involved intraperitoneal administration of PBAP-Her2 (150
441 μg/mouse), followed by the administration of Kadcyla (3 mg/kg) or Adcetris (3 mg/kg)

via tail vein injection 24 hours later. Both treatments were administered once a week for two consecutive cycles. Mice were euthanized 7 days after the second ADCs treatment for tissue and tumor collection (Fig. 7A). The results demonstrated that only the PBAP-Her2 + Kadcyla group exhibited significant tumor control and regression (Fig. 7B). Immunohistochemistry (IHC) results demonstrated that PBAP-Her2 specifically infiltrated tumor tissues. Notably, significant ADC drug infiltration within the tumor tissue was only observed in the PBAP-Her2 + Kadcyla treatment group, indicating a synergy effect between PBAP-Her2 and the ADC treatment in promoting targeted delivery (Fig. 7C). Immunofluorescence analysis further confirmed that only the PBAP-Her2 + Kadcyla group exhibited notable tumor regression or control. Tumor sections revealed clear co-localization of PBAP-Her2 with PD-L1 on tumor cells. Furthermore, Kadcyla was observed to enter tumor cells exclusively in the PBAP-Her2 + Kadcyla group, where it was internalized by the tumor cells, whereas no intracellular ADCs uptake was detected in the control groups, which included Kadcyla monotherapy or the PBAP-Her2 + Adcetris combination therapy group (PBAP-Her2 + Adcetris). This selective intracellular uptake highlights the enhanced targeting and delivery of the ADC, facilitated by PBAP-Her2-mediated tumor cell engagement (Fig. 7D, Fig. S10).

Hematoxylin and eosin (H&E), reviewed by two independent pathologists, revealed no significant histopathological damage to major organs, including the heart, liver, spleen, and lungs in the experimental group, indicating a favorable safety profile. However, an increase in multinucleated giant cells was observed in the spleens, with particularly pronounced accumulation in the PBAP-Her2 + Kadcyla group, suggesting a potential immune response or inflammatory process associated with the

466 experimental treatment. This finding warrants further investigation into the renal
467 effects and the role of PD-L1 expression in mediating off-target responses (Fig. 7E).
468 In summary, these findings underscore the potent anti-tumor efficacy of PBAP-Her2
469 in combination with ADCs, showing the capability to effectively eradicate solid
470 tumors.

471

472 **3. Discussion**

473 Overcoming tumor immune evasion remains a critical challenge in cancer
474 immunotherapy. One of the major barriers is the loss or downregulation of
475 tumor-specific antigens, which impairs cytotoxic T lymphocyte (CTL) recognition
476 and limits the effectiveness of targeted therapies. To address this challenge, we
477 developed a modular immune-bridging strategy utilizing PD-L1 binding antigen
478 presenters (PBAP) that capitalize on pre-existing antiviral humoral immunity for
479 tumor eradication. Our approach leverages PBAP that selectively bind PD-L1-positive
480 tumor cells, displaying non-tumor viral antigens recognized by antibodies induced
481 through vaccination or prior viral exposure.

482 This innovative "tumor tagging" mechanism achieves dual functions: it not only
483 blocks PD-1 inhibitory signaling by competitive binding, but also redirects
484 antibody-dependent effector functions, primarily through NK cells, to the TME via
485 ADCC. Unlike traditional antigen-targeting therapies, our system is tumor-agnostic
486 and antigen-independent, allowing it to overcome the limitations posed by tumor
487 heterogeneity and antigen loss, broadening its application across various tumor types.

488 In the context of PBAP-gE, we utilized antibodies elicited by recombinant zoster
489 vaccines, demonstrating potent synergy with CAR-T cell-delivered PBAP in both *in*

vitro and *in vivo* models. Notably, mechanistic studies revealed that the anti-tumor effect was primarily driven by vaccine-induced antibodies rather than $CD8^+$ T cells, as evidenced by B cell and $CD8^+$ T cell depletion experiments. Unlike oncolytic viruses or bacterial vectors for antigen delivery, our PBAP system offers a pharmacologically simpler, safer, and more controllable approach, particularly when combined with activation-dependent expression through CAR-T platforms.

To accelerate the clinical translation of PBAP, a critical need remains for the development of delivery systems that minimize off-target effects and immunogenicity. Currently, CAR-T cells co-expressing PBAP represent a highly promising fourth-generation CAR-T technology. Compared to protein-based biologics, they encounter fewer regulatory obstacles, thereby facilitating more rapid progression toward clinical application. These CAR-T cells drive the expression of PBAP through the NFAT promoter, thereby directly linking PBAP expression directly to CAR-T cell activation. Moreover, in the future, tumor-specific promoters, such as NR4A2 or RGS16, which are selectively expressed in tumor-infiltrating T cells, could be utilized for the spatially restricted expression of PBAP.[55] This approach offers targeted, localized tumor engagement, minimizing systemic toxicity and positioning PBAP as a promising partner in viral infection- or vaccine-based therapies. From a translational perspective, the PBAP platform is highly versatile, enabling combination with licensed vaccines and personalized approaches for patients with pre-existing antiviral immunity. Furthermore, the PBAP platform is inherently extensible. Beyond PD-L1, future iterations could target other immune-suppressive ligands (e.g., CD155, B7-H3, SIRPα) or tumor-associated surface glycans, thereby expanding the scope of its applicability across diverse tumor types and resistance mechanisms.

4. Conclusion

PBAP provides a flexible, tumor-agnostic platform that harnesses vaccine-induced immunity to enhance antibody-based therapies. By addressing antigen loss and heterogeneity, PBAP expands the arsenal of immunotherapeutic strategies and paves the way for translational development of humoral redirection platforms.

5. Experimental Section

Ethics Statements: The Ethics Review Board of Shenzhen Hospital of Southern Medical University (SHSMU) and Shenzhen TOP Biotechnology Co., Ltd (TOP) approved this study. Animal experiments were carried out in strict compliance with the guidelines and approved by Ethics Committee of SHSMU and TOP on Laboratory Animal Care (Assurance Number: 20240030, TOP-IACUC-2025-0092).

Cell Lines and Culture Conditions: Human cancer cell lines of MDA-MB-231 (RRID: CVCL_0062), HEK 293T (RRID: CVCL_0063) and HEK 293F (RRID: CVCL_6642) were obtained from the American Type Culture Collection (ATCC). Mouse cell lines of 4T1 (RRID: CVCL_0125) and B16-F10 (RRID: CVCL_0159) were obtained from the American Type Culture Collection (ATCC). Immortalized mouse NK cells (KIL C.2, RRID: CVCL_HC59) were obtained from Applied Biological Materials Inc. B16-F10-Trop2^{+} (B16-Trop2) cells were established by infecting B16-F10 with lentivirus carrying Trop2-IRES-GFP, followed by sorting GFP^{high} cells (BD FACS Aria II). B16-F10-fLuc (B16-fLuc) were established by infecting B16-F10 cells with lentiviruses carrying luciferase-IRES-RFP, followed by sorting RFP^{high} cells to enable bioluminescence *in vivo* imaging. MDA-MB-231, 293T, B16-F10, B16-F10-Trop2^{+}(B16-Trop2) and B16-F10-fLuc(B16-fLuc) cells were cultured in DMEM medium (Invitrogen) supplemented with 10% FBS, 1%

penicillin–streptomycin and 2 mM l-glutamine (Invitrogen). HEK 293F cells were cultured in Union 293 medium (Union Bio) supplemented with 8 mM glutamine (ThermoFisher) and 1% penicillin-streptomycin (ThermoFisher). 4T1 cells were cultured in RPMI-1640 medium with 10% FBS, 2 mM l-glutamine (Invitrogen) and 1% penicillin–streptomycin (Invitrogen). KIL C.2 cells were cultured in PriGrow V medium (Applied Biological Materials) supplemented with 30% fetal bovine serum (Sigma Aldrich), 2 mM l-glutamine, 50 ng/ml recombinant mouse stem cell factor (SCF, R&D Systems), 25 ng/ml recombinant mouse IL-7 (R&D Systems) and 1% penicillin–streptomycin (Invitrogen). 1×10^6 cells/mL KIL C.2 cells were incubated with culture medium containing 20 ng/mL recombinant mouse IL-2 (R&D Systems) overnight before use.

All cell lines except 293F cells were maintained in a humidified atmosphere containing 37 ℃ and 5% carbon dioxide and passaged two or three times a week. 293F cells were cultured at 37 ℃, 8% carbon dioxide and 130 rpm speed in orbital shaker. All cell lines were authenticated by STR profiling and tested regularly for mycoplasma contamination using a MycoAlert Mycoplasma Detection kit (Lonza) and were only used when tested negative for contamination.

Animal Models: Specific-pathogen-free (SPF) 6- to 8-weeks-old male C57BL/6 mice were purchased from Guangdong Medical Laboratory Animal Center (GDMLAC) . Specific-pathogen-free (SPF) 6- to 8-weeks-old male NSG mice were purchased from Shanghai Model Organisms Center, Inc. Only male mice were used because the experimental design required repeated blood collections, and males generally tolerate serial bleeding better than females, thereby improving survival rates and minimizing animal loss. All mice were housed with ad libitum access to food and water in SPF barrier facilities at the Laboratory Animal Center of SHSMU and TOP.

For ethical reasons, mice that exhibited a loss of body weight exceeding 20% and ceased to consume food and water were humanely euthanized, serving as an endpoint to minimize any potential distress.

Plasmid Construction: 293F cells expressing protein-related plasmid: DNA sequences of sPD-1-gE, GE, GE-53-50A, sPD-1-Her2 with 6 × His-tagged at C-terminal and PBAP-gE, PBAP-Her2 were codon-optimized and synthesized by Sangon Biotech into pcDNA3.1 plasmid. sPD-1-gE and PBAP-gE were designed by fusing the extracellular domain of PD-1 (sPD-1) to viral antigen domain GE with a linker that was predicted and structurally optimized based on AlphaFold 3 modeling. PBAP-gE was further engineered to incorporate an Fc domain (IgG2) and a signal peptide. Similarly, sPD-1-Her2 and PBAP-Her2 were designed by fusing the soluble extracellular domain of PD-1 (sPD-1) to IV domain of Her2 using a optimized linker sequence and appending an Fc domain (IgG1, L234A, L235A) at the C-terminus. In addition, PBAP-Her2 was also engineered to include an Fc domain and a signal peptide. GE-53-50A were designed by fusing the extracellular domain of VZV gE (aa 31-544) to the I53-50A component to enable antigen display on the corresponding NP carriers, with a signal peptide and 6 × His-tagged at C-terminal Tag. Competent Escherichia coli BL21(DE3) expressing protein-related plasmid: DNA sequences of I53-50B with 6 × His-tagged at C-terminal were synthesized by Sangon Biotech into pET28a vector.

Two anti-Trop2 CAR constructs (Trop2-CAR, Trop2-CAR-PBAP) and one control CAR construct (anti-CD19) were synthesized and cloned into the third-generation retrovirus plasmid backbones under the regulation of LTR promoter. All CAR constructs contained a mouse CD28 transmembrane and intracellular costimulatory domain in tandem with a mouse CD3ζ intracellular signaling domain. To construct a

vector encoding PBAP-gE in murine anti-Trop2 CAR (Trop2-CAR-PBAP), the PBAP-gE gene was inserted into the *BamHI* and *ClaI* restriction enzyme sites of the MIGR1 retroviral vector, and NFAT promoter was inserted between CAR and PBAP-gE genes. The sequences of CD19 CAR were obtained from publicly available sequences for FMC63.

Protein Expression and Purification: sPD-1-gE, PBAP-gE, GE, GE-53-50A, sPD-1-Her2 and PBAP-Her2 were produced in 293F cells grown in suspension using Union 293 medium (Union Bio) at 37 ℃, 8% carbon dioxide and 130 rpm speed in orbital shaker. Cultures were transiently transfected with PEI (Union Bio) at a cell density of 2.0–3.0 × 10^6 cells/ml and incubated for 3-4 days. After centrifugation to remove cellular debris, supernatants containing His-tagged proteins (sPD-1-gE, GE, GE-I53-50A, sPD-1-Her2, PBAP-Her2) were applied to Ni-NTA resin (Vazyme) and eluted with imidazole-containing Tris buffer. PBAP-gE and PBAP-Her2 were further purified on HiTrap Protein A HP columns (Vazyme). Purified proteins were concentrated and buffer-exchanged into Tris buffer; concentrations were determined by BCA assay and protein purity was assessed by Coomassie Blue staining.

I53-50B was expressed and purified from BL21 *E.coli* (Biosharp) prokaryotic expression system induced by isopropyl-D-thiogalactopyranoside (IPTG, Biosharp). The bacterial cultures were harvested and lysed in Tris buffer (20 mM Tris, 50 mM NaCl, pH 7.5). After harvested and lysed by sonication, the supernatants were collected and incubated with Ni-NTA agarose (Vazyme) to enrich His-tagged I53-50B，followed by protein elution with Imidazole -containing Tris buffer. The purified I53-50B proteins were concentrated and buffer-replaced with conventional Tris buffer. The concentration of I53-50B was determined by BCA assay and Coomassie Blue staining were executed to confirm the purity.

For conjugation, I53-50B and gE-I53-50A were mixed at a 3:1 mass ratio and incubated overnight at 2-8 ℃. Uncoupled gE-I53-50A and excessive I50-53B were removed from the conjugated NP by size-exclusion chromatography (SEC) using a Superdex 200 Increase 10/300 GL column (Cytiva) pre-equilibrated with 20 mM Tris-HCl, 25% sucrose w/v, pH 7.4 on the AKTA system (Cytiva). After separation, the conjugated gE-I53-50 nanoparticles were analysed on Coomassie Blue staining, western blotting, size-exclusion chromatography (SEC), and transmission electron microscopy (TEM), to determine the coupling efficiency by densitometry as previously described. Besides, the bacterial endotoxins in nanoparticle were quantified by tachypleus amebocytelysate test (less than 100 EU/mg).

PBAP Inhibition of PD-L1 Binding to PD-1 in Vitro: ELISA Blocking Activity Detection of PBAP-Her2: 96-well plates were coated with 2μg/ml human PD-L1 (ECD, His Tag, SinoBiological, 10084-H08H) protein in carbonate buffer overnight at 2-8 ℃. The next day, the plates were blocked with 2% BSA for 1 hours at 37 ℃ and then washed with 0.05% PBST. Subsequently, PBAP-Her2 (10 μg/well) with a dilution ratio of 1:10, was added to the wells. Four hours later, PD-L1 monoclonal antibody (SinoBiological, 10084-MM33) was added to the coated plates at dilution of 1:10000, followed by incubation for 2 hours at 37 ℃. After incubation, the plates were washed with 0.05% PBST and incubated with Goat anti-Mouse IgG, HRP secondary antibody (SinoBiological, SSA007) for 1 hour at 37 ℃. Finally, TMB substrate (SinoBiological, SEKCR01) was added and incubated for 10-15 minutes, followed by stopping reaction with stop solution (Solarbio) after sufficient development. The absorbance was measured at 450 nm using a microplate reader. The blocking effect of the antibody on PD-1/PD-L1 binding was determined based on the absorbance values.

For the ELISA blocking activity detection of PBAP-gE, the same procedure was followed with the following modifications: human PD-L1 (ECD, His Tag, SinoBiological, 10084-H08H) protein was replaced with mouse PD-L1 (ECD, His Tag, SinoBiological, 50010-M08H), PBAP-Her2 (1 μg/well and 10 μg/well) was replaced with PBAP-gE (1 μg/well and 10 μg/well), PD-L1 monoclonal antibody (SinoBiological, 10084-MM33) was replaced with PD-L1 monoclonal antibody (SinoBiological, B50010-R678), and Goat anti-Mouse IgG, HRP secondary antibody (SinoBiological, SSA007) was replaced with Goat anti-Rabbit IgG, HRP secondary antibody (SinoBiological, SSA004) . All other steps remained unchanged.

flow cytometer Detection of PBAP-Her2: MDA-MB-231-PD-L1 cells were plated in a 96-well plate at a density of 1×10^5 cells per well and maintained in a humidified atmosphere containing 37 ℃ and 5% carbon dioxide overnight. The next day, PBAP-Her2 (10 μg/well) was added to the wells. Four hours later, PD-L1 monoclonal antibody (SinoBiological, 10084-MM33) was added to the coated plates, with a dilution of 1:5000, followed by incubation for 2 hours, the cells were washed with PBS and incubated with PE-labeled goat anti-mouse IgG (H+L) fluorescent secondary antibody (Invitrogen, P-852) for 30 minutes on ice. Finally, after another wash with PBS, the cells were analyzed using a flow cytometer to assess the blocking activity of the antibody on the PD-1/PD-L1 signaling pathway by measuring the fluorescence intensity of the antibody-cell binding.

For the flow cytometer blocking activity detection of PBAP-gE, the same procedure was followed with the following modifications: MDA-MB-231-PD-L1-OE cells were replaced with 4T1-PD-L1-OE cells, PBAP-Her2 (10 μg/well) was replaced with PBAP-gE (10 μg/well), PD-L1 monoclonal antibody (SinoBiological, 10084-MM33) was replaced with PD-L1 monoclonal antibody (SinoBiological, B50010-R678),

PE-labeled goat anti-mouse IgG (H+L) fluorescent secondary antibody (Invitrogen, P-852) was replaced with goat anti-Rabbit IgG (H+L) fluorescent secondary antibody (Invitrogen, P-2771MP). All other steps remained unchanged.

In Vitro ADCC Reporter Assay: The MDA-MB-231-PD-L1-OE and MDA-MB-231-PD-L1-KO cells were harvested and seeded into a white opaque 96-well assay plate with 1.0×10^4 cells in 100 μl of RPMI-1640 medium with 2% FBS per well separately, followed by incubation at 37 ℃, 5% carbon dioxide overnight (16-24h). Subsequently, an overdosage of PBAP (10 μg/well) was added to the wells. Four hours later, Trastuzumab (MCE, HY-P9907) was serially diluted in the assay medium (RPMI-1640 medium with 2% FBS) at a starting concentration of 4 μg/well, with a dilution ratio of 1:4. Jurkat-FcγRIIIa (Vazyme, ADCC) and Jurkat-FcγRIIa (Vazyme, ADCP) effector cells were then added to the plate at a density of 1.0×10^5 cells per well. Jurkat-FcγRIIIa (Vazyme, ADCC) and Jurkat-FcγRIIa (Vazyme, ADCP) effector cells were then added to the plate at a density of 1.0×10^5 cells per well. The plate was incubated at 37 ℃, 5% carbon dioxide for 6 h. After incubation, 50 μL of Bio-Lite reagent (Vazyme) was added to each well and relative luciferase units (RLU) were measured using the GloMax Navigator (Promega).

To further elucidate the effects of PBAP and Trastuzumab on ADCC and ADCP activity, three control conditions were established: (1) no addition of PBAP, (2) no addition of Trastuzumab, and (3) no addition of either PBAP or Trastuzumab.

CRISPR Knockout of PD-L1: CRISPR/Cas9 technology was used to knockout PD-L1 in 4T1 cells and MDA-MB-231 cells. The sgRNA sequences targeting mouse (sgRNA: GTATGGCAG-CAACGTCACGA) and human PD-L1 (sgRNA: ACCGTTCAGCAAATGCCAGT)were designed using the online CRISPR design

690 tool (Benchling) and transfected into 4T1 cells and MDA-MB-231 cells using
691 Lipofectamine 3000 (Invitrogen) separately. Knockout cells were selected with
692 puromycin (10 μg/mL) for 10 days and screened by flow cytometer for PD-L1
693 negative populations.

694 ***Cytotoxicity Assays:*** The ability of KIL C.2 cells to kill tumor target cells via
695 PBAP-gE and LZ901 vaccined murine serum was measured by lactate dehydrogenase
696 (LDH) assay. Briefly, The 4T1-PD-L1-OE and 4T1-PD-L1-KO cells were harvested
697 and seeded into a transparent 96-well assay plate (V bottom) with 1.0×10^4 cells in
698 100 μl of PriGrow V medium with 30% FBS per well separately, followed by
699 incubation at 37 ℃, 5% carbon dioxide overnight (16-24 h). Subsequently, an
700 overdosage of PBAP-gE (10 μg/well) was added to the wells. Four hours later,
701 LZ901-vaccinated murine serum (Endpoint titer = 3.4) was diluted 100-fold and then
702 added to each well at a volume of 100 μl. KIL C.2 cells containing 20 ng/mL IL-2
703 (R&D Systems) and IL-7 (R&D Systems) were then added to the plate at a start
704 density of 8.0×10^4 cells/well, with a dilution ratio of 1:2. The plate was incubated at
705 37 ℃, 5% carbon dioxide for 24 h.

706 LDH release was measured using the CytoTox96 nonradioactive cytotoxicity assay
707 (Promega) according to the manufacturer's instructions. Absorbance values from
708 wells containing effector cells alone and target cells alone were detected and
709 subtracted as background from the co-culture values. Wells containing target cells
710 alone were lysed with a lysis reagent for 30 minutes at 37 ℃, and the resulting
711 luminescence was set as 100% lysis. Cytotoxicity was calculated using the following

712 formula: $\%\text{Cytotoxicity} = \frac{(\text{Experimental} - \text{Effector spontaneous} - \text{Target spontaneous})}{(\text{Target maximum} - \text{Target spontaneous})} \times 100\%$

713 To evaluate the *in vitro* cytotoxicity of Trop2-CAR-PBAP cells against target cells,
714 the B16-Trop2 cells were harvested and seeded into a transparent 96-well assay plate

(V bottom) with 1.0×10^4 cells in 100 μl of 1640 medium with 10% FBS per well separately, followed by incubation at 37 ℃, 5% carbon dioxide overnight (16-24 h). Subsequently, Trop2-CAR cells (negative control) and Trop2-CAR-PBAP cells containing 20 ng/mL IL-2 (R&D Systems) were then added to the plate at a start density of 8.0×10^4 cells/well, with a dilution ratio of 1:2. The plate was incubated at 37 ℃, 5% carbon dioxide for 24 h. LDH release was measured using the CytoTox96 nonradioactive cytotoxicity assay (Promega) according to the manufacturer's instructions and cytotoxicity was calculated using the same formula as described above.

Similarly, the cytotoxic activity of NK cells against tumor target cells mediated by PBAP-Her2 and Trastuzumab was evaluated using the LDH assay. Briefly, the MDA-MB-231-PD-L1-OE and MDA-MB-231-PD-L1-KO cells were harvested and seeded into a transparent 96-well assay plate (V bottom) with 1.0×10^4 cells in 100 μl of RPMI-1640 medium with 10% FBS per well separately, followed by incubation at 37 ℃, 5% carbon dioxide overnight (16-24 h). Subsequently, an overdosage of PBAP-Her2 (10 μg/well) was added to the wells. Four hours later, Trastuzumab (1 μg/well) was added. NK cells were then added to the plate at a start density of 8.0×10^4 cells/well, with a dilution ratio of 1:2. The plate was incubated at 37 ℃, 5% carbon dioxide for 24 h. LDH release was measured using the CytoTox96 nonradioactive cytotoxicity assay (Promega) according to the manufacturer's instructions and cytotoxicity was calculated using the same formula as described above.

To evaluate the *in vitro* cytotoxicity of ADC drugs (Kadcyla) in combination with PBAP-Her2 against target cells, a CCK8 assay was performed. Briefly, the MDA-MB-231 cells were harvested and seeded into a transparent 96-well assay plate

(V bottom) with 1.0×10^4 cells in 100 µl of RPMI-1640 medium with 10% FBS per well separately, followed by incubation at 37 ℃, 5% carbon dioxide overnight (16-24 h). Subsequently, an overdosage of PBAP-Her2 (10 µg/well) was added to the wells. Four hours later, ADC drugs (Kadcyla or Adcetris) were added at various concentrations (0.1, 1, 10, 100, and 1000 ng/ml). The plates were incubated at 37 ℃ with 5% carbon dioxide for 24 h. Cytotoxicity was assessed using the CCK8 assay according to the manufacturer's instructions (Dojindo Molecular Technologies), with absorbance measured at 450 nm using a microplate reader. The percentage of cell viability was calculated relative to untreated control cells.

Negative Stain Electron Microscopy: Transmission electron microscopy (TEM) grids of gE-I53-50 nanoparticles were subjected to negative-stain electron microscopy at Shenzhen Bay Laboratory. Briefly, 3.5 µL of each sample (0.1 mg/mL) was applied to glow-discharged TEM grids coated with a thin continuous carbon film and stained with 2% uranyl acetate. Imaging was performed using a Hitachi HT7800 microscope operating at an acceleration voltage of 120 kV. Images were recorded at a magnification of 80,000× and a defocus of 1.5 µm.

For sample preparation, gE-I53-50 nanoparticles were first diluted to 0.1 mg/mL in 20 mM Tris pH 7.0, 150 mM NaCl. Then, 3.5 µL of the sample was applied to freshly glow-discharged 300-mesh carbon grids. After incubation for 1 min, excess liquid was blotted away with filter paper (Whatman). The grids were then stained by applying 10 µL of 2% uranyl acetate, followed by blotting; this staining step was repeated three times, with the third staining incubated for 1 min. Subsequently, the grids were washed three times with 10 µL of ultrapure water, and excess liquid was blotted away. Finally, the grids were air-dried for 1 min before imaging. Prepared grids were examined under a Hitachi HT7800 electron microscope at a magnification of 80,000×.

765 ***Dynamic Light Scattering:*** Dynamic Light Scattering (DLS) was used to
766 measure hydrodynamic diameter (Dh) and % Polydispersity (%Pd) of gE-I53-50
767 nanoparticle samples on an UNcle Nano-DSF (UNchained Laboratories). Sample was
768 applied to a 8.8 µL quartz capillary cassette (UNi, UNchained Laboratories) and
769 measured with 10 acquisitions of 5 s each, using auto-attenuation of the laser.
770 Increased viscosity due to 4.5% v/v glycerol in the gE-I53-50 nanoparticle buffer was
771 accounted for by the UNcle Client software in Dh measurements.

772 ***Transfection and Virus Production:*** Retroviral vectors encoding Trop2-CAR,
773 Trop2-CAR-PBAP and CD19-CAR were produced by co-transfecting HEK-293T
774 cells with the packaging plasmids (PCLECO) separately. Transfection was carried out
775 using a standard calcium phosphate precipitation method, following a protocol
776 optimized for efficient virus production. After 48 hours of incubation, viral
777 supernatants were collected and filtered through a 0.45 µm filter to remove cell debris.
778 To concentrate the lentivirus, the supernatants were subjected to ultracentrifugation at
779 25,000 × g for 2 hours at 4°C, and the resultant viral pellet was resuspended in a small
780 volume of phosphate-buffered saline (PBS). The concentrated lentivirus was aliquoted
781 and stored at -80°C for future use.

782 ***Mouse CAR-T Cell Generation:*** To generate mouse CAR-T cells, T cells were
783 isolated from the spleen and lymph nodes of C57BL/6 mice using the mouse T cell
784 isolation kit (STEMCELL Biotec). These isolated T cells were activated with
785 immobilized anti-CD3e antibody (5 µg/mL, eBioscience) and anti-CD28 (2 µg/mL,
786 eBioscience) antibodies in the presence of murine IL-2 (ProSpec) in RPMI-1640
787 medium containing 10% FBS, 1% penicillin-streptomycin, and 55 nM
788 β-Mercaptoethanol. After 24 h activation, the T cells were transduced with retroviral
789 supernatants at an optimized multiplicity of infection (MOI), and spinoculation was

performed at 800 × g for 90 minutes at 32℃ to enhance transduction efficiency. Following transduction, the cells were cultured and expanded in RPMI-1640 medium with 10% FBS and murine IL-2 (100 IU/mL) for 3 days. The CAR expression was determined with flow cytometer analysis, and the functionality of the CAR-T cells was evaluated by cytotoxicity assays and cytokine release assays.

PBAP Secretion Assay of Trop2-CAR-PBAP: To evaluate the PBAP secretion of Trop2-CAR-PBAP cells, 1.0 × 10^6 Trop2-CAR cells (negative control) and Trop2-CAR-PBAP cells were aliquoted and cultured with B16-F10 cells at a ratio of 2:1 under 1640 medium with 10% FBS. The supernatants of the culture medium were sampled after 48 h. To assess PBAP-secreting capabilities after consistent antigen stimulation, 1.0 × 10^6 Trop2-CAR cells (negative control) and Trop2-CAR-PBAP cells were aliquoted and cultured with B16-Trop2 cells at a ratio of 2:1 under 1640 medium with 10% FBS. The supernatants of the culture medium were sampled after 48 h. Concentrations of PBAP were determined by ELISA (His Tag ELISA Detection Kit, L00435, GenScript), under the instructions of the manufacturer.

Tumor Infiltrated B cell Separation and Identification: To isolate and culture B cells from B16-Trop2 tumor tissue, tumors were collected in PBS and homogenized through 70 mm strainers, and incubated in ACK lysis buffer to remove red blood cells (RBCs), followed by centrifuging and passing through a 40 mm strainer to obtain single cells. To enrich for B cells, CD19-MicroBeads were used (Miltenyi Biotec, 130-121-301), followed by magnetic cell sorting (MACS). The positively selected B cells are then cultured in RPMI-1640 medium supplemented with 10% FBS, 1% penicillin-streptomycin, and 50 μM β-mercaptoethanol. 1.0 × 10^6 cells are incubated at 37 ℃ and 5% carbon dioxide. B cells coculture with 5 ng/mL IL-4 (Beyotime, P5916) and 2 μg/mL CD40L (Biolegend, 797404) for antibody secretion.

In Vivo Syngeneic Tumor Models: For *in vivo* experiments testing PBAP-gE delivered via CAR-T cells or intratumoral injection against B16-Trop2 tumor cells in murine tumor models, 6-8 week-old male C57BL/6 mice were immunized with the recombinant zoster vaccine LZ901 on Days 0 and 21 (5 μg/mouse/dose). On Day 27, sera were collected. On Day 28, mice were subcutaneously inoculated with B16-Trop2 cells. When average tumor volumes reached ~100 mm^3, treatments were administered as per the experimental design. Tumor sizes were meticulously monitored throughout the study period, and blood samples and tumor tissues were collected for in-depth analysis when mice were euthanized.

To investigate the anti-tumor activity of PBAP-gE mediated primarily by vaccine-induced antibodies or gE-specific $CD8^+$ T cells, C57BL/6 mice were immunized with the LZ901 vaccine on Days 0 and 21 (5 μg/mouse/dose). On Day 28, B16-fLuc cells were subcutaneously injected into the mice. B cell depletion was achieved by intraperitoneal injection of anti-mouse CD19 (clone 1D3), CD22 (clone CY34.1), and B220 (clone RA3-6B2) antibodies (150 μg/mouse/antibody) on Day 33. Similarly, for $CD8^+$ T cell depletion, anti-mouse CD8 antibody (clone 16-0081-85) was administered intraperitoneally. On Day 35, mice received intratumoral injections of PBAP-gE (150 μg/mouse). Tumor growth was monitored using an *in vivo* imaging system, and the images were analyzed using Live Imaging Software (Perkin Elmer).

To further evaluate the relationship between endogenous antibody levels and the therapeutic efficacy of PBAP-based treatments, GE subunit vaccine and GE-I53-50 VLP vaccine were introduced. C57BL/6 mice were divided into six groups (n = 8 per group): saline control, GE subunit vaccine, LZ901 vaccine, GE-I53-50 VLP vaccine, and two GE-I53-50 VLP groups with either B cell or $CD8^+$ T cell depletion. Vaccinations were administered on Days 0 and 21 (5 μg/mouse/dose), with sera

collected on Day 27. Tumors were established by subcutaneous injection of B16-Trop2 cells on Day 28. Depleting antibodies were administered on Day 33, and PBAP-gE was injected intratumorally on Day 35 (150 μg/mouse).

In Vivo Xenograft Models: NSG mice were subcutaneously inoculated with 5×10^6 MDA-MB-231 cells (in 100 μL PBS). Mice were assigned to the following treatment groups: PBAP-Her2 control, Kadcyla control, PBAP-Her2 + Adcetris (CD30-targeting ADC) control, and PBAP-Her2 + Kadcyla. Tumor growth was monitored regularly, and when the average tumor volume reached approximately 100 mm^3, treatments were initiated according to the experimental design. PBAP-Her2 (150 μg/mouse) was administered intraperitoneally, followed 24 hours later by Kadcyla (3 mg/kg) via tail vein injection. For the control groups, Adcetris (3 mg/kg) was administered via the same route and schedule. Both treatments were given once a week for two consecutive cycles. Mice were euthanized 7 days after the second ADC treatment for tissue and tumor collection. Upon euthanasia, tumor weights were measured, and the hearts, livers, spleens, lungs, kidneys, and tumor tissues were collected for subsequent in-depth analysis.

Enzyme Linked Immunosorbent Assay (ELISA): For test the anti-gE IgG in blood samples and B cells of C57BL/6 mice, recombinant gE antigen was coated on high-binding 96-well plates at 2 ug/mL overnight at 2-8 ℃. After washing with 0.05% PBST, plates were blocked with 2% BSA in PBST for 1 h. Immunized mice serum were serially diluted and added into each well in duplicate followed by incubating at room temperature for 1 h. After washing with PBST, the detection of gE-specific IgG antibody in serum of BALB/c was conducted through adding HRP-conjugated goat anti-mouse (SinoBiological, SSA007) respectively at dilution of 1:10000 and incubating for another 1 h. After washing with PBST, HRP substrate TMB solution

(SinoBiological, SEKCR01) was added, followed by stopping reaction with stop solution (Solarbio) after sufficient development. Plates were immediately read at 450 nm and the data was analyzed using GraphPad Prism 8.0 software for non-linear regression to calculate endpoint titers.

Flow Cytometer: The spleens and tumors were collected in PBS and homogenized through 70 mm strainers, and incubated in ACK lysis buffer to remove red blood cells (RBCs), followed by centrifuging and passing through a 40 mm strainer to obtain single cells.

For the staining of lymphocyte surface markers, cells were stained with indicated fluorochrome-conjugated monoclonal antibodies for 30 min within PBS containing 0.5% BSA on ice. The following indicated antibodies were used: FITC anti-GGGGS (Hycells, GS-ARFT), FITC anti-mouse CD90.2 (Biolegend, 105306), PE anti-mouse CD4 (Biolegend, 100408), APC anti-mouse CD8a (Biolegend, 100712), Pacific Blue anti-mouse CD19 (Biolegend, 152416), PE-Cyanine7 anti-mouse CD11b (Biolegend, 101215), PE-Dazzle 594 anti-mouse NK1.1 (Biolegend, 108747).

For the staining of lymphocyte intracellular cytokines, cells were performed with the 1 mL Permeabilization buffer (Invitrogen, 00-8333-56). Then Brilliant Violet 421 anti-mouse IFN-γ (Biolegend, 505829) was used for the intracellular staining and the flow cytometer analysis.

Histopathology and Immunohistochemistry: MDA-MB-231 cells xenograft NSG mice were euthanized and major tissues, included heart, liver, spleen, lung, kidney, were collected and fixed in 4% paraformaldehyde bufferfor 48 h, followed by embedding with paraffin. Longitudinal sections were performed and the sections (3-4 μm) were stained with hematoxylin and eosin (H&E). Images were captured with Digital Slide Scanner (3DHISTECH, Pannoramic MIDI).

Tumor sections (3 μm thick) were stained with Her2 specific antibody (Sinobiological, 310184-T08, Rabbit PAb) to assess PBAP-gE infiltration and anti-human Fab (Abcam, ab771, Mouse Mab) to evaluate the penetration and localization of ADCs within the tumor tissue. IHC was performed with HRP-conjugated secondary antibodies and visualized with DAB substrate (Vector Laboratories). Stained slides were quantified using ImageJ software.

Immunofluorescence Staining and Imaging: Briefly, the tumors were excised and prepared using the Swiss roll technique, fixed with BD Cytoperm/Cytofix (BD Bioscience, 554722) solution (diluted with PBS at 1:2) overnight at 2-8 ℃, followed by dehydrated in 30% sucrose for 12-16 h before embedding in OCT compound (Sakura Finetek, 4583). 8-10 μm sections were prepared by CRYOSTAR NX5 (Thermo). The experiment assessed PBAP-gE infiltration and ADC localization within tumor tissue using three-color fluorescence staining. Paraffin-embedded tissue sections were deparaffinized, followed by antigen retrieval and endogenous peroxidase blocking. The sections were incubated with anti-human PD-L1 (Abcam, ab279293, Mouse Mab) to label PD-L1 expression on tumor cells, Her2-specific antibody (Sinobiological, 310184-T08, Rabbit PAb) to detect PBAP-gE infiltration, and anti-human Fab (Abcam, ab771, Mouse Mab) to evaluate the penetration and localization of ADCs within the tumor tissue. Signal amplification was achieved using HRP-conjugated secondary antibodies and iF488/555-TSA working solution. DAPI was used for nuclear counterstaining, and autofluorescence was quenched. The sections were then mounted with anti-fluorescence quenching mounting medium, and fluorescence microscopy was performed to observe and capture images. The experiment also included an antibody elution step to ensure signal specificity. Fluorescence three-color staining was conducted using the Servicebio® TSAPLus

Fluorescent Triple-Color Staining Kit (G1236).

Statistical Analysis: All experiments were performed in triplicates or more, and data are presented as the mean ± SD. Statistical significance was determined using one-way ANOVA with Tukey's post-test or unpaired t-test or Kruskal-Wallis test where appropriate. A p-value of less than 0.05 was considered statistically significant.

Supporting Information

Figs. S1 to S10

Acknowledgements

The authors thank Zhaofeng Huang (Sun Yat-sen University, Guangzhou, China) for B16-F10-Trop2^{+} (B16-Trop2) and B16-F10-fLuc (B16-fLuc) cells. The authors thank Xin Wang (Southern University of Science and Technology, Shenzhen, China) for Jurkat-FcγRIIIa (ADCC) and Jurkat-FcγRIIa (ADCP) effector cells. The authors thank Dr. Gang Fu and Dr. Huifang Yan at the Structural Biology Core Facility of Shenzhen Medical Academy of Research and Translation (SMART) for negative-stain electron microscopy.

Funding

This work was supported by Shenzhen Science and Technology Program (JCYJ20250604190324033) and Natural Science Foundation of China (82003252) to F.Z; Guangdong Basic and Applied Basic Research Foundation of China (2023A1515220144) to W.W; Natural Science Foundation of China (82202986) and Natural Science Foundation of Guangdong Province (2023A1515220017, 2025A1515010135) to J.T; Natural Science Foundation of Guangdong Province

(2024A1515012867) and Doctor "Sailing" project of Science and Technology Department of Guangzhou (2024A04J3291) to T.L; Sanming Project of Medicine in Shenzhen (No. SZSM202311032) to L.H.

Conflict of Interest

F.Z., N.N.L., and X.L.L. are inventors on patents related to the use of PBAP. The remaining authors declare no competing financial interests.

Author contributions

H.X.G., Lijuan Lu, X.X., Y.L., and D.H. contributed equally to this work; F.Z. supervised the project; F.Z., W.W., S.S., and Y.X.designed the study; H.G., Lijuan Lu, X.X., Y.L., D.H., H.F., G.T., C.S., Z.Z, N.L., X.L., J.T., L.H., and T.L. conducted the experiments; H.G., Lijuan Lu, X.X., Y.L., D.H., W.F., C.L., H.F., G.T., C.S., Z.Z, N.L., X.L., J.T., L.H., and S.S. acquired data; F.Z., H.G., Lijuan Lu, W.F., X.X., Y.L., L.P., Lu Lu, and Y.Z. analyzed data; F.Z., H.G., L.L., W.F., X.X., Y.L., D.Z., Z.F., and Y.X. wrote the manuscript.

Data Availability Statement

The data that support the findings of this study are available from the corresponding author upon reasonable request.

References

1 Elhanani, O., Ben-Uri, R. & Keren, L. Spatial profiling technologies illuminate the tumor microenvironment. *Cancer Cell* **41**, 404-420, doi:10.1016/j.ccell.2023.01.010 (2023).

2 Steele, N. G. *et al.* Multimodal Mapping of the Tumor and Peripheral Blood Immune Landscape in Human Pancreatic Cancer. *Nat Cancer* **1**, 1097-1112, doi:10.1038/s43018-020-00121-4 (2020).

3 Zhang, Y. & Zhang, Z. The history and advances in cancer immunotherapy: understanding the characteristics of tumor-infiltrating immune cells and their therapeutic implications. *Cell Mol Immunol* **17**, 807-821, doi:10.1038/s41423-020-0488-6 (2020).

4 Jhunjhunwala, S., Hammer, C. & Delamarre, L. Antigen presentation in cancer: insights into tumour immunogenicity and immune evasion. *Nat Rev Cancer* **21**, 298-312, doi:10.1038/s41568-021-00339-z (2021).

5 Chiou, S. H. *et al.* Global analysis of shared T cell specificities in human non-small cell lung cancer enables HLA inference and antigen discovery. *Immunity* **54**, 586-602.e588, doi:10.1016/j.immuni.2021.02.014 (2021).

6 Lowery, F. J. *et al.* Molecular signatures of antitumor neoantigen-reactive T cells from metastatic human cancers. *Science* **375**, 877-884, doi:10.1126/science.abl5447 (2022).

7 Meier, S. L., Satpathy, A. T. & Wells, D. K. Bystander T cells in cancer immunology and therapy. *Nat Cancer* **3**, 143-155, doi:10.1038/s43018-022-00335-8 (2022).

8 Oliveira, G. *et al.* Phenotype, specificity and avidity of antitumour CD8(+) T cells in melanoma. *Nature* **596**, 119-125, doi:10.1038/s41586-021-03704-y (2021).

9 Rosato, P. C. *et al.* Virus-specific memory T cells populate tumors and can be repurposed for tumor immunotherapy. *Nat Commun* **10**, 567, doi:10.1038/s41467-019-08534-1 (2019).

10 Scheper, W. *et al.* Low and variable tumor reactivity of the intratumoral TCR repertoire in human cancers. *Nat Med* **25**, 89-94, doi:10.1038/s41591-018-0266-5 (2019).

11 Simoni, Y. *et al.* Bystander CD8(+) T cells are abundant and phenotypically distinct in human tumour infiltrates. *Nature* **557**, 575-579, doi:10.1038/s41586-018-0130-2 (2018).

12 Li, S. *et al.* Bystander CD4(+) T cells infiltrate human tumors and are phenotypically distinct. *Oncoimmunology* **11**, 2012961, doi:10.1080/2162402x.2021.2012961 (2022).

13 Caushi, J. X. *et al.* Transcriptional programs of neoantigen-specific TIL in anti-PD-1-treated lung cancers. *Nature* **596**, 126-132, doi:10.1038/s41586-021-03752-4 (2021).

14 Duhen, T. *et al.* Co-expression of CD39 and CD103 identifies tumor-reactive CD8 T cells in human solid tumors. *Nat Commun* **9**, 2724, doi:10.1038/s41467-018-05072-0 (2018).

15 Roy, D. G. *et al.* Adjuvant oncolytic virotherapy for personalized anti-cancer vaccination. *Nat Commun* **12**, 2626, doi:10.1038/s41467-021-22929-z (2021).

16 Zhong, L. *et al.* Hyperacute rejection-engineered oncolytic virus for interventional clinical trial in refractory cancer patients. *Cell* **188**, 1119-1136.e1123, doi:10.1016/j.cell.2024.12.010 (2025).

17 Taha, Z. *et al.* Complementary dual-virus strategy drives synthetic target and cognate T-cell engager expression for endogenous-antigen agnostic immunotherapy. *Nat Commun* **15**, 7267, doi:10.1038/s41467-024-51498-0 (2024).

18 Redenti, A. *et al.* Probiotic neoantigen delivery vectors for precision cancer immunotherapy. *Nature* **635**, 453-461, doi:10.1038/s41586-024-08033-4 (2024).

19 Chen, X. *et al.* An oncolytic virus delivering tumor-irrelevant bystander T cell epitopes induces anti-tumor immunity and potentiates cancer immunotherapy. *Nat Cancer* **5**, 1063-1081, doi:10.1038/s43018-024-00760-x (2024).

20 Dong, H. *et al.* Tumor-associated B7-H1 promotes T-cell apoptosis: a potential mechanism of immune evasion. *Nat Med* **8**, 793-800, doi:10.1038/nm730 (2002).

21 Chen, D. S. & Mellman, I. Elements of cancer immunity and the cancer-immune set point. *Nature* **541**, 321-330, doi:10.1038/nature21349 (2017).

22 Li, C. W. *et al.* Eradication of Triple-Negative Breast Cancer Cells by Targeting Glycosylated PD-L1. *Cancer Cell* **33**, 187-201.e110, doi:10.1016/j.ccell.2018.01.009 (2018).

23 Park, J. E. *et al.* Anti-tumor effects of NK cells and anti-PD-L1 antibody with antibody-dependent cellular cytotoxicity in PD-L1-positive cancer cell lines. *J Immunother Cancer* **8**, doi:10.1136/jitc-2020-000873 (2020).

24 Tan, J. *et al.* Anti-PD-L1 antibody enhances curative effect of cryoablation via antibody-dependent cell-mediated cytotoxicity mediating PD-L1(high)CD11b(+) cells elimination in hepatocellular carcinoma. *Acta Pharm Sin B* **13**, 632-647, doi:10.1016/j.apsb.2022.08.006 (2023).

25 Boyerinas, B. *et al.* Antibody-Dependent Cellular Cytotoxicity Activity of a Novel Anti-PD-L1 Antibody Avelumab (MSB0010718C) on Human Tumor Cells. *Cancer Immunol Res* **3**, 1148-1157, doi:10.1158/2326-6066.Cir-15-0059 (2015).

26 Powles, T. *et al.* Avelumab Maintenance Therapy for Advanced or Metastatic Urothelial Carcinoma. *N Engl J Med* **383**, 1218-1230, doi:10.1056/NEJMoa2002788 (2020).

27 Winer, E. P. *et al.* Pembrolizumab versus investigator-choice chemotherapy for metastatic triple-negative breast cancer (KEYNOTE-119): a randomised, open-label, phase 3 trial. *Lancet Oncol* **22**, 499-511, doi:10.1016/s1470-2045(20)30754-3 (2021).

28 Adams, S. *et al.* Pembrolizumab monotherapy for previously treated metastatic triple-negative breast cancer: cohort A of the phase II KEYNOTE-086 study. *Ann Oncol* **30**, 397-404, doi:10.1093/annonc/mdy517 (2019).

29 Dong, Y. *et al.* Novel bispecific antibody-drug conjugate targeting PD-L1 and B7-H3 enhances antitumor efficacy and promotes immune-mediated antitumor responses. *J Immunother Cancer* **12**, doi:10.1136/jitc-2024-009710 (2024).

30 Xiao, D. *et al.* Development of bifunctional anti-PD-L1 antibody MMAE conjugate with cytotoxicity and immunostimulation. *Bioorg Chem* **116**, 105366, doi:10.1016/j.bioorg.2021.105366 (2021).

31 Patnaik, A. *et al.* Phase 1 study of SGN-PDL1V, a novel, investigational vedotin antibody–drug conjugate directed to PD-L1, in patients with advanced solid tumors (SGNPDL1V-001, trial in progress). *Journal of Clinical Oncology* **40**, TPS3154-TPS3154, doi:10.1200/JCO.2022.40.16_suppl.TPS3154 (2022).

32 Shan, Y. *et al.* Preclinical activity of HLX43, a PD-L1-targeting ADC in multiple PD-1/PD-L1 refractory/resistant models. *Annals of Oncology* (2023).

33 Li, H. Y. *et al.* Bispecific antibody targeting both B7-H3 and PD-L1 exhibits superior antitumor activities. *Acta Pharmacol Sin* **44**, 2322-2330, doi:10.1038/s41401-023-01118-2 (2023).

34 Hu, C. *et al.* 1201-B Characterization of a novel bifunctional anti-PD-L1 antibody-drug conjugate for the treatment of solid tumors. *Journal for ImmunoTherapy of Cancer* **11**, A1847-A1847, doi:10.1136/jitc-2023-SITC2023.1201-B (2023).

35 Amanna, I. J., Carlson, N. E. & Slifka, M. K. Duration of humoral immunity to common viral and vaccine antigens. *N Engl J Med* **357**, 1903-1915, doi:10.1056/NEJMoa066092 (2007).

36 Vink, P. *et al.* Immunogenicity and safety of the adjuvanted recombinant zoster vaccine in patients with solid tumors, vaccinated before or during chemotherapy: A randomized trial. *Cancer* **125**, 1301-1312, doi:10.1002/cncr.31909 (2019).

37 Lasagna, A. *et al.* The immunogenicity and the safety of the adjuvanted glycoprotein E (gE)-based recombinant vaccine against herpes zoster (RZV) in cancer patients during immunotherapy. *Hum Vaccin Immunother* **19**, 2288282, doi:10.1080/21645515.2023.2288282 (2023).

38 Junak, S. *et al.* Phase II Study of Responses to Vaccination in Pediatric Cancer Survivors Following Standard-of-Care Non-HSCT Chemotherapy. *Pediatr Blood Cancer* **72**, e31611, doi:10.1002/pbc.31611 (2025).

39 Zengin, E. & Sarper, N. Humoral immunity to diphtheria, tetanus, measles, and hemophilus influenzae type b in children with acute lymphoblastic leukemia and response to re-vaccination. *Pediatr Blood Cancer* **53**, 967-972, doi:10.1002/pbc.22135 (2009).

40 Patel, S. R. *et al.* Revaccination of children after completion of standard chemotherapy for acute leukemia. *Clin Infect Dis* **44**, 635-642, doi:10.1086/511636 (2007).

41 Ercan, T. E. *et al.* Antibody titers and immune response to diphtheria-tetanus-pertussis and measles-mumps-rubella vaccination in children treated for acute lymphoblastic leukemia. *J Pediatr Hematol Oncol* **27**, 273-277, doi:10.1097/01.mph.0000163214.37147.5a (2005).

42 Quan, Y. *et al.* Comparison of the Immunogenicity of the LZ901 Vaccine and HZ/su Vaccine in a Mouse Model. *Vaccines (Basel)* **12**, doi:10.3390/vaccines12070775 (2024).

43 Jin, P. F. *et al.* Immunogenicity and safety of a recombinant gE-Fc fusion protein subunit vaccine for herpes zoster in adults ≥50 years of age: a randomised, active-controlled, non-inferiority trial. *Nat Commun* **16**, 7590, doi:10.1038/s41467-025-62800-z (2025).

44 Zou, F. *et al.* Engineered triple inhibitory receptor resistance improves anti-tumor CAR-T cell performance via CD56. *Nature Communications* **10**, doi:10.1038/s41467-019-11893-4 (2019).

45 Liu, B. F. *et al.* Chimeric Antigen Receptor T Cells Guided by the Single-Chain Fv of a Broadly Neutralizing Antibody Specifically and Effectively Eradicate Virus Reactivated from Latency in CD4+ T Lymphocytes Isolated from HIV-1-Infected Individuals Receiving Suppressive Combined Antiretroviral Therapy. *Journal of Virology* **90**, 9712-9724, doi:10.1128/jvi.00852-16 (2016).

46 Zou, F. *et al.* The CD39+ HBV surface protein-targeted CAR-T and personalized tumor-reactive CD8+ T cells exhibit potent anti-HCC activity. *Molecular Therapy* **29**, 1794-1807, doi:10.1016/j.ymthe.2021.01.021 (2021).

47 Zou, F. *et al.* Moderate expression of CD39 in GPC3-CAR-T cells shows high efficacy against hepatocellular carcinoma. *Frontiers of Medicine* **18**, 708-720, doi:10.1007/s11684-024-1071-9 (2024).

48 Qiao, Y. D. *et al.* Enhancement of CAR-T cell activity against cholangiocarcinoma by simultaneous knockdown of six inhibitory membrane proteins. *Cancer Communications* **43**, 788-807, doi:10.1002/cac2.12452 (2023).

49 Liu, B. F. *et al.* Broadly neutralizing antibody derived CAR T cells reduce viral reservoir in individuals infected with HIV-1. *Journal of Clinical Investigation* **131**, doi:10.1172/jci150211 (2021).

50 Ma, X. *et al.* Nanoparticle Vaccines Based on the Receptor Binding Domain (RBD) and Heptad Repeat (HR) of SARS-CoV-2 Elicit Robust Protective Immune Responses. *Immunity* **53**, 1315-1330.e1319, doi:10.1016/j.immuni.2020.11.015 (2020).

51 Yuan, Y. *et al.* A bivalent nanoparticle vaccine exhibits potent cross-protection against the variants of SARS-CoV-2. *Cell Rep* **38**, 110256, doi:10.1016/j.celrep.2021.110256 (2022).

52 Chen, R. *et al.* Development of Receptor Binding Domain (RBD)-Conjugated Nanoparticle Vaccines with Broad Neutralization against SARS-CoV-2 Delta and Other Variants. *Adv Sci (Weinh)* **9**, e2105378, doi:10.1002/advs.202105378 (2022).

53 Zhang, X. *et al.* Improvement of a SARS-CoV-2 vaccine by enhancing the conjugation efficiency of the immunogen to self-assembled nanoparticles. *Cell Mol Immunol* **18**, 2042-2044, doi:10.1038/s41423-021-00736-2 (2021).

54 Li, Y. *et al.* A nanoparticle vaccine displaying varicella-zoster virus gE antigen induces a superior cellular immune response than a licensed vaccine in mice and non-human primates. *Front Immunol* **15**, 1419634, doi:10.3389/fimmu.2024.1419634 (2024).

55 Chen, A. X. Y. *et al.* Rewiring endogenous genes in CAR T cells for tumour-restricted payload delivery. *Nature* **644**, 241-251, doi:10.1038/s41586-025-09212-7 (2025).

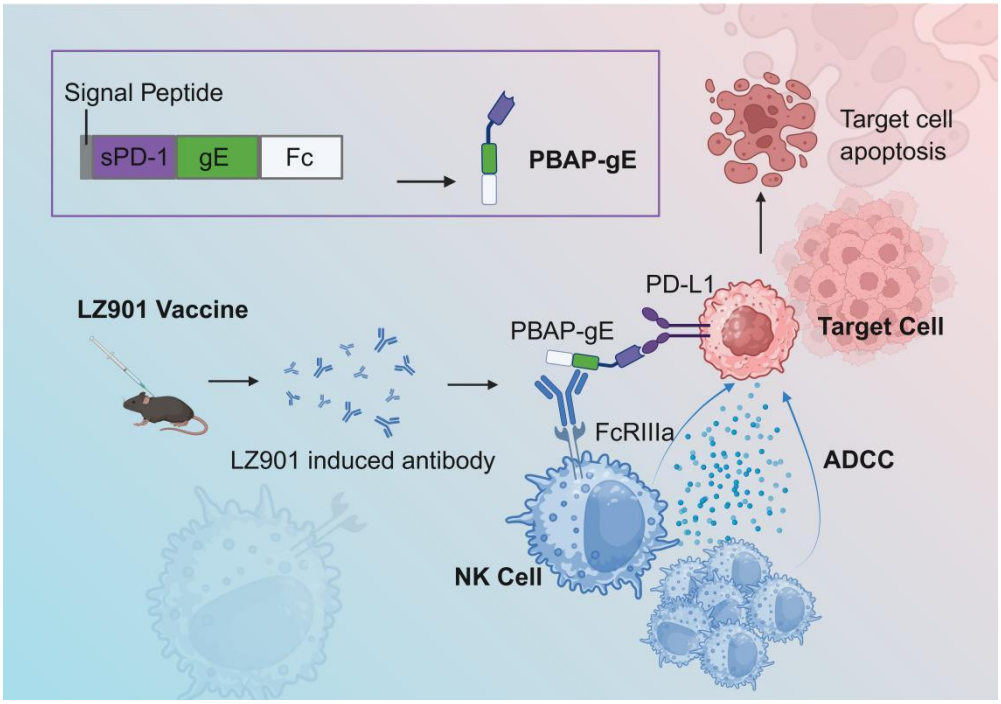

Scheme 1. Mechanism of PBAP-gE Complex Combined with LZ901 Vaccine in Enhancing NK Cell-Mediated Anti-Tumor Efficacy.

The PBAP-gE complex specifically binds to PD-L1 on PD-L1-positive tumor cells via its sPD-L1 domain, thereby labeling these cells with the gE antigen. Subsequently, the LZ901 vaccine activates the immune system to produce gE - specific antibodies (anti-gE antibodies), which exert their effects through two distinct pathways. Firstly, these antibodies directly bind to the FcγRIIIa receptors on NK cells, providing activation signals. Secondly, they specifically bind to the PBAP-gE complex already present on tumor cells. Together, these dual actions trigger NK cell-mediated ADCC, significantly augmenting NK cells' ability to target and destroy PD-L1-positive tumor cells. Created with BioRender.com.

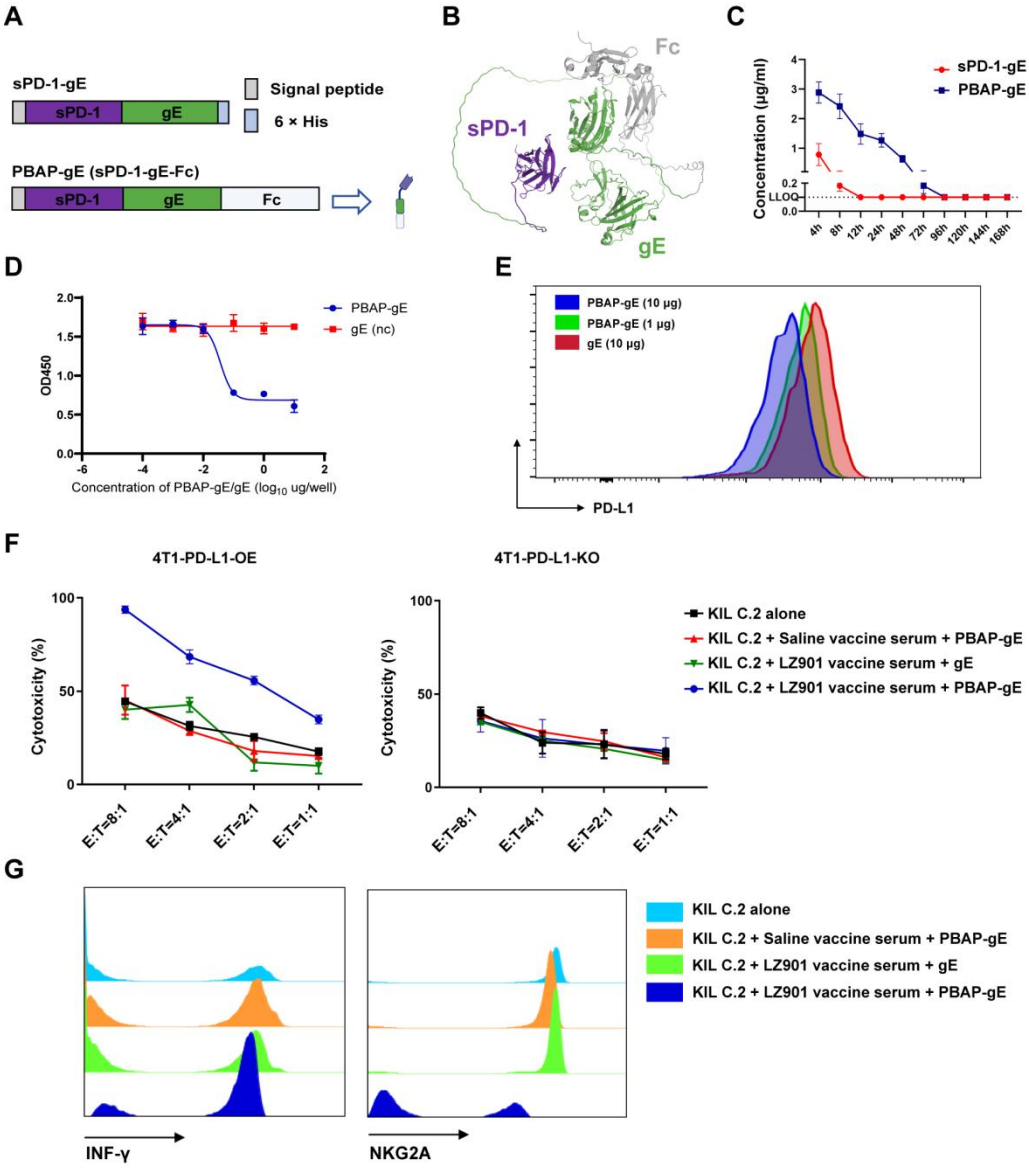

Fig. 1. Serum from Herpes Zoster Vaccine (LZ901)-immunized Mice Enhances PBAP-Mediated ADCC Against PD-L1$^+$ Tumor Cells *In Vitro*.

A) Schematic diagram of the sPD-1-gE and PBAP-gE fusion protein. The sPD-1-gE construct consists of sPD-1 fused to gE. The PBAP-gE construct comprises sPD-1-gE fused with an Fc domain (sPD-1-gE-Fc).

B) Structural modeling of PBAP-gE with AlphaFold 3.

C) Pharmacokinetic profiles of sPD-1-gE and PBAP-gE following intravenous injection into C57BL/6J mice (n=3 mice/group, 100 μg/mice).

D) The binding inhibition of PBAP-gE on PD-L1/PD-1 interaction was assessed by ELISA. The absorbance was measured at 450 nm to determine the blocking effect.

E) The fluorescence intensity of the antibody-cell binding was analyzed using a flow cytometer to assess the blocking effect on the PD-1/PD-L1 pathway.

F) *In vitro* cytotoxicity assay. KIL C.2 cells were co-incubated with PBAP-gE and serum from LZ901-immunized mice, against 4T1-PD-L1-OE tumor cells and 4T1-PD-L1-KO cells. KIL C.2 cells, KIL C.2 cells co-incubated with gE and serum from LZ901-immunized mice, and KIL C.2 cells co-incubated with PBAP-gE and serum from saline vaccine-immunized mice were used as controls. Representative of 2 independent experiments.

G) Flow cytometer analysis of IFN-γ expression and inhibitory receptor (NKG2A) levels in KIL C.2 cells. Representative of 3 independent experiments.

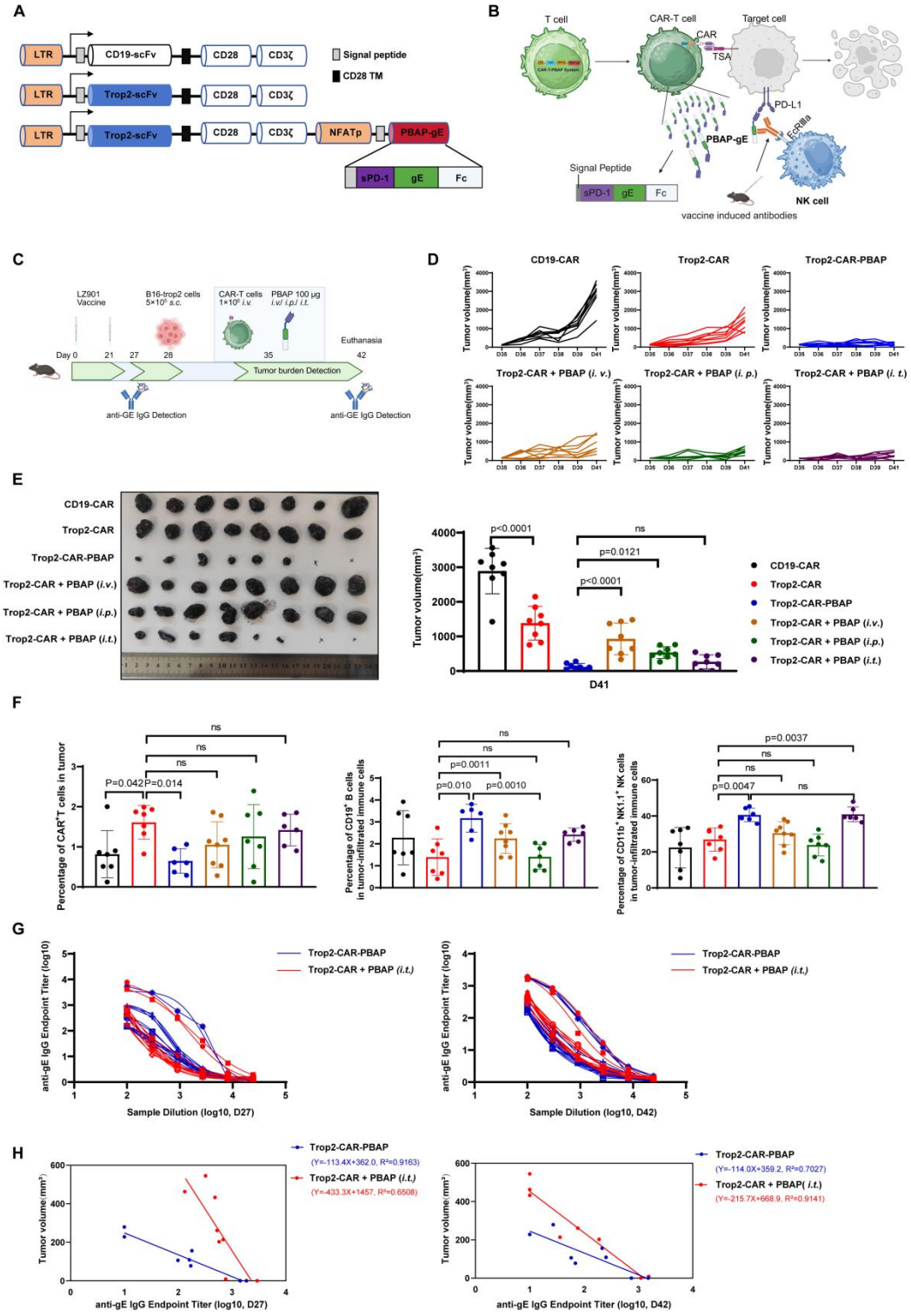

Fig. 2. Trop2-CAR-T Cells Coexpressing PBAP-gE or Combined with PBAP-gE Intratumoral Injection Induces Tumor Regression in LZ901-Vaccinated Mice.

A) Schematic representation of the CAR construct. The VH and VL domains are ligated with the CD28 transmembrane (TM) domain, followed by the CD3ζ intracellular domain (control group). The experimental group incorporates an

additional PBAP-gE module, driven by the NFAT promoter at the C-terminus to enable tumor-specific expression.

B) Diagram of the CAR-T-PBAP system, which integrates a CAR module with a PBAP-gE expression cassette driven by the NFAT promoter. Upon recognition of tumor antigens by the CAR ectodomain on T cells, PBAP-gE is expressed and secreted. PBAP-gE bridges vaccine- or natural viral infection-induced antibodies bound to FcγRIIIa^{+} NK cells with PD-L1^{+} tumor cells, triggering antibody-dependent cellular cytotoxicity (ADCC) and subsequent tumor cell lysis. Created with BioRender.com.

C) Overview of Experimental Design. C57BL/6J mice (n=8 mice/group) received LZ901 vaccine (5 μg/dose) on Days 0 and 21, with serum collected for anti-gE IgG detection on Day 27. On Day 28, 5×10^5 B16-F10/Trop2 cells were subcutaneously implanted. When tumors reached 100 mm^3 (Day 35), mice were infused with a single dose of CAR-T cells, with or without PBAP-gE, via intravenous (*i.v.*), intraperitoneal (*i.p.*), or intratumoral (*i.t.*) injection. Terminal serum was collected on Day 42 for anti-gE IgG analysis. Created with BioRender.com.

D) Tumor volumes were measured every 1-2 days across all groups, and all mice were euthanized on Day 42.

E) Representative images of tumors are shown on the left, with tumor volumes at the experimental endpoint shown in the right panel. The PBAP-coexpressing CAR-T cell group demonstrated tumor regression comparable to the intratumoral injection group.

F) Analysis of tumor-infiltrating immune cells by flow cytometer, revealed that both the Trop2-CAR-PBAP and Trop2-CAR + PBAP (*i.t.*) groups had significantly elevated frequencies of B cells and NK cells.

For panels E and F, data are presented as the mean ± s.d, n=8. Statistical significance was determined using one-way ANOVA. ns indicates not significant ($P > 0.05$).

G) The binding affinity of serum from LZ901-vaccinated mice with gE at Days 27 and 42 was analyzed by ELISA in the Trop2-CAR-PBAP treatment group and Trop2-CAR + PBAP treatment group.

H) Correlation analysis of tumor volume with gE-specific IgG antibody levels (Endpoint titer) at Days 27 and 42 between Trop2-CAR-PBAP treatment group and Trop2-CAR + PBAP-gE (*i.t.*) treatment group.

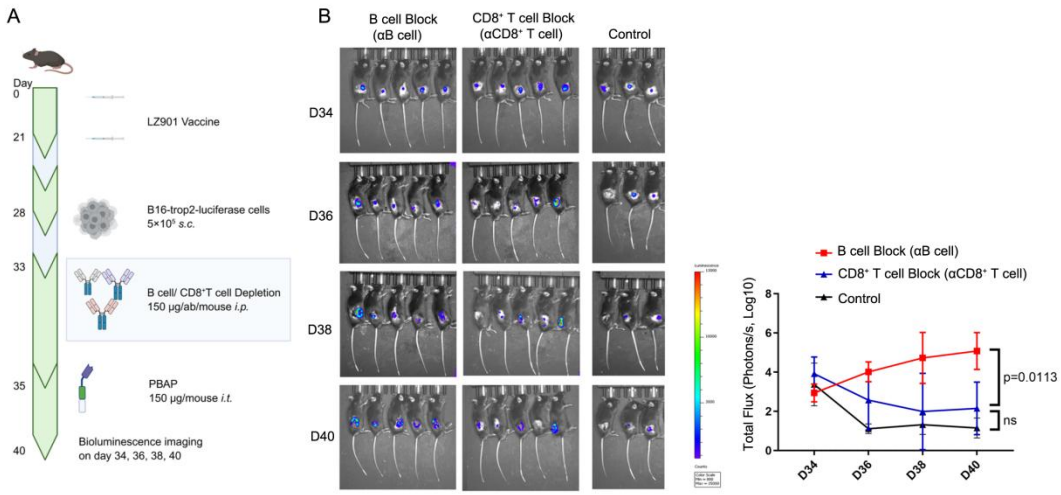

Fig. 3. PBAP-gE Elicits a Robust Anti-Tumor Immune Response, Predominantly Mediated by NK Cells through gE-Specific Antibody Production by B Cells.

A) Experimental design to assess the contributions of antibody versus $CD8^+$ T cells in PBAP-gE-mediated tumor suppression. C57BL/6J mice (n=5 mice/group) were immunized with the LZ901 vaccine (5 μg/dose) on Days 0 and 21. On Day 28, 5×10^5 B16-Trop2-luciferase cells (luciferase-IRES-RFP^+) were subcutaneously engrafted. B cell depletion was achieved on Day 33 via anti-CD19, anti-CD22, and anti-B220 antibodies, while $CD8^+$ T cell depletion was induced by anti-CD8 antibodies. On Day 35, mice received intratumoral injections of PBAP-gE (150 μg/mouse), and tumor growth was monitored using an in vivo imaging system (IVIS), allowing for real-time tracking of tumor dynamics. Created with BioRender.com.

B) In tumor-bearing mice, *in vivo* imaging results before and after depletion of B cells or $CD8^+$ T cells were obtained. The group with depletion of B cells and the group with depletion of $CD8^+$ T cells each included 5 mice, while the control group contained 3 mice.

For panel B, data are presented as the mean ± s.d. Statistical significance was determined using Kruskal-Wallis test. ns indicates not significant ($P > 0.05$).

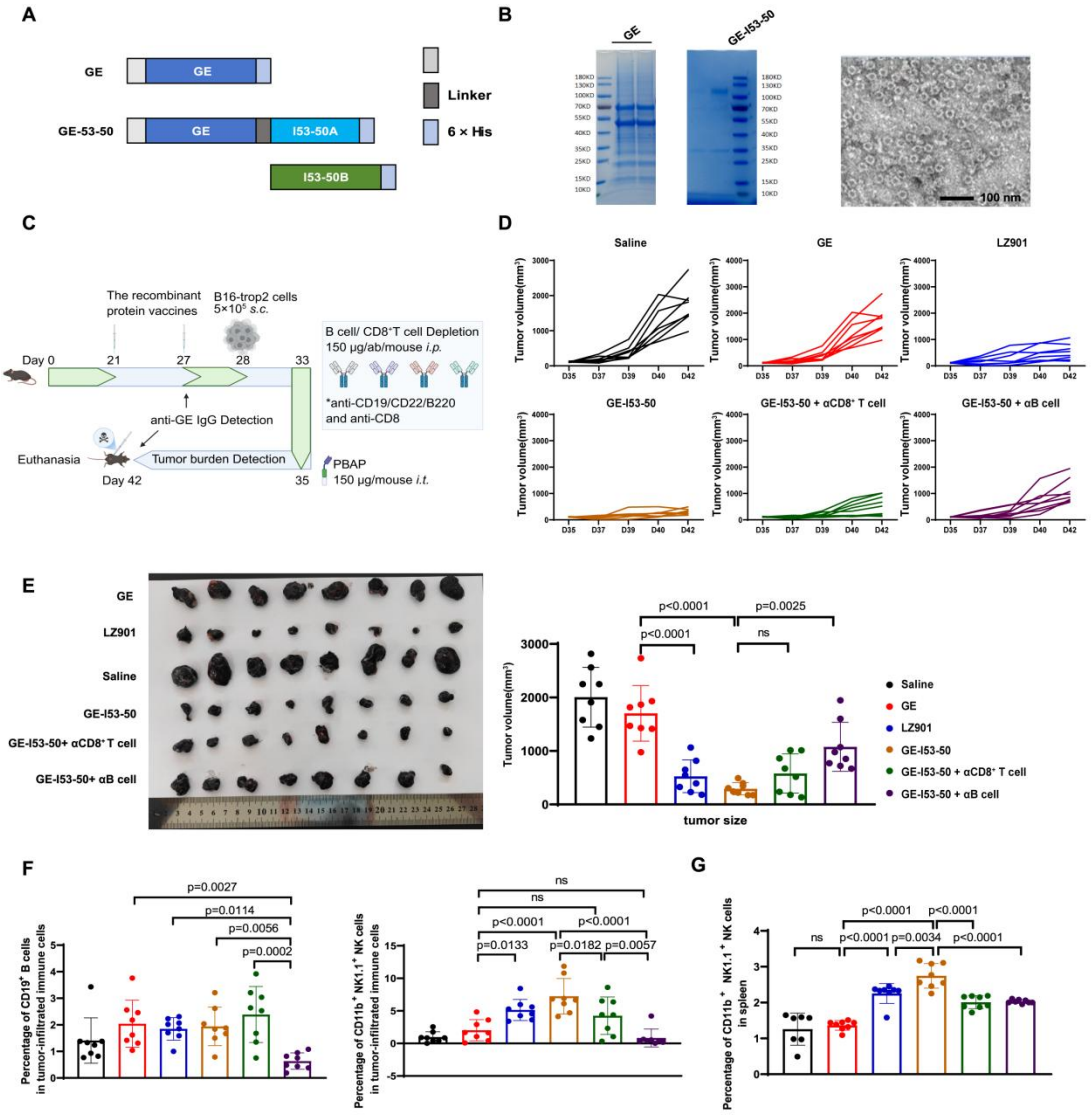

Fig. 4. The Titers of Antibody Dominate PBAP Anti-Tumor Activity.

A) Schematic representation of the other two recombinant protein vaccines used in the study: the low-immunogenicity gE subunit vaccine and the high-immunogenicity GE-I53-50 virus-like particle (VLP) vaccine formulated by I53-50B and GE-I53-50A. Scale bars, 100 nm.

B) Coomassie Blue staining of gE and GE-I53-50 nanoparticles confirming the expression and purity of the recombinant proteins (left panel). Transmission electron microscopy (TEM) image showing the morphology of GE-I53-50 nanoparticles (right panel).

C) Overview of Experimental Design. C57BL/6J mice (n=8 mice/group) were immunized with the vaccines (5 μg/dose) on Days 0 and 21. Serum collected on Day 27 was analyzed for anti-gE IgG levels. On Day 28, 5×10^5 B16-F10/Trop2 cells were subcutaneously engrafted. On Day 33, B cell and $CD8^+$ T cell depletion was

performed on Day 33 using intraperitoneal injections of anti-CD19/CD22/B220 (αB cell depletion, 150 μg/mouse each) and anti-CD8 antibodies ($\alpha CD8^+$ T cell depletion, 150 μg/mouse each). On Day 35, PBAP-gE (150 μg/mouse) was administered intratumorally, and tumor progression was monitored. Tumor volumes were measured every 1-2 days until Day 42, when mice were euthanized for analysis of tumor burden and serum anti-gE IgG levels. Created with BioRender.com.

D) Tumor growth curves were plotted for the six experimental groups: saline control, gE subunit vaccine, LZ901 vaccine, GE-I53-50 VLP vaccine, GE-I53-50 VLP + $\alpha CD8^+$ T cell depletion, and GE-I53-50 VLP + αB cell depletion. Corresponding anti-gE-specific IgG antibody levels are shown on the right, illustrating the correlation between vaccine-induced antibody responses and tumor growth suppression.

E) Representative tumor images are shown on the left, with tumor volumes at the experimental endpoint shown in the right panel. The GE-I53-50 VLP vaccine groups showed significant tumor regression.

F) Analysis of tumor-infiltrating immune cells by flow cytometer, revealed that NK cells frequencies were significantly elevated in the tumor tissue of mice vaccinated with LZ901 or GE-I53-50 VLP, treated with PBAP-gE.

G) Analysis of NK cells in the spleen by flow cytometer revealed that NK cells frequencies were significantly elevated in the spleen of mice vaccinated with LZ901 or GE-I53-50 VLP, treated with PBAP-gE.

For panels E, F and G, data are presented as the mean ± s.d, n=8. Statistical significance was determined using one-way ANOVA. ns indicates not significant ($P > 0.05$).

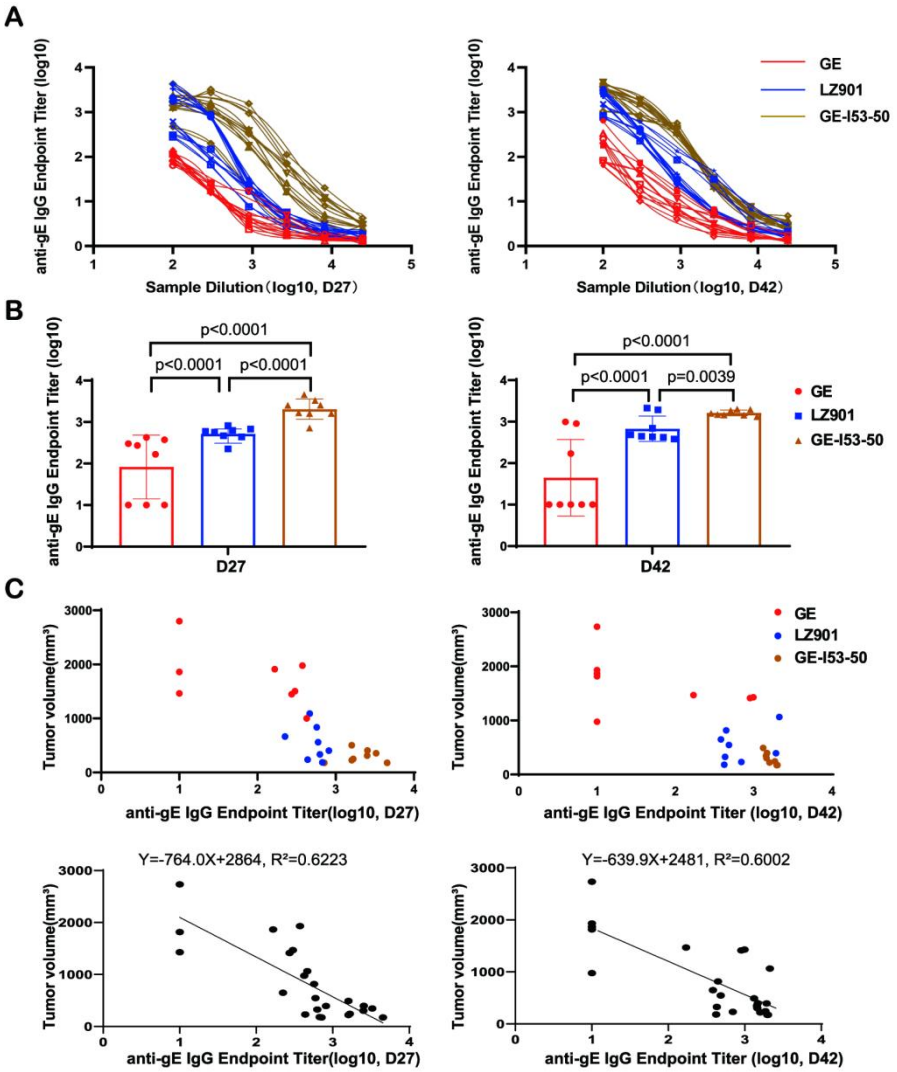

Fig. 5. Tumor Burden Inversely Correlated with gE-specific IgG Antibody Levels (Endpoint titer) among gE Subunit Vaccine, LZ901 Vaccine, and GE-I53-50 VLP Vaccine Treatment Groups.

A) The binding affinity of serum from LZ901-vaccinated mice with gE was analyzed by ELISA among gE subunit vaccine, LZ901 vaccine, and GE-I53-50 VLP vaccine treatment groups.

B) The serum gE-specific IgG antibody levels (Endpoint titer) at Days 27 and 42 in mice immunized with the gE subunit vaccine, LZ901 vaccine, and GE-I53-50 VLP vaccine.

C) Correlation analysis of tumor burden with serum gE-specific IgG antibody levels (Endpoint titer) at Days 27 and 42 in mice immunized with the gE subunit vaccine, LZ901 vaccine, and GE-I53-50 VLP vaccine.

For panel B, data are presented as the mean ± s.d. Statistical significance was determined using one-way ANOVA.

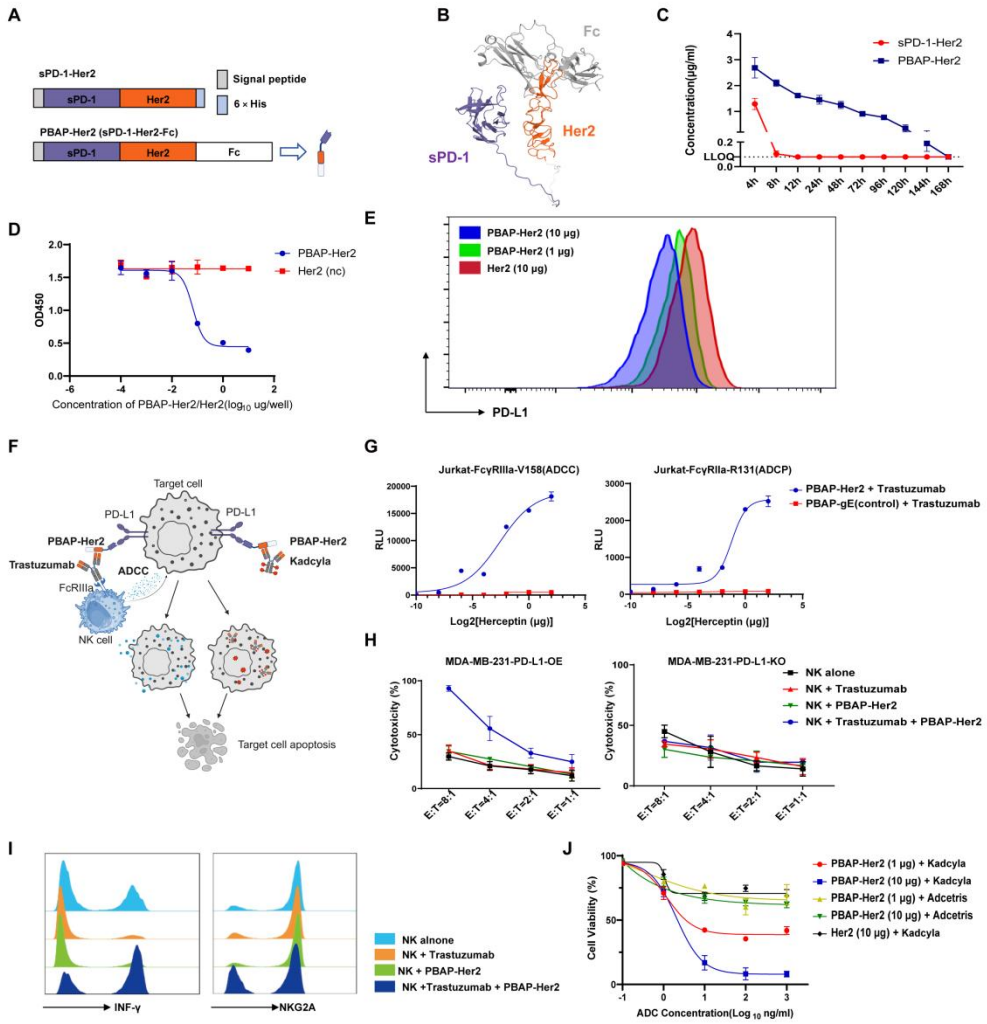

Fig. 6. PBAP Incorporating Tumor-specific Antigens Enhance Synergistic Anti-tumor Activity with Commercial Antibodies and ADCs *In Vitro*.

A) Schematic representation of the design of sPD-1-Her2 and PBAP-Her2 (sPD-1-Her2-Fc). PBAP-Her2 is engineered by fusing the extracellular domain of human PD-1 (sPD-1) with Domain IV of the Her2 protein, followed by the addition of an Fc region to enhance stability and extend half-life.

B) Structural modeling of PBAP-Her2 with AlphaFold 3.

C) Pharmacokinetic profiles of sPD-1-Her2 and PBAP-Her2 following intravenous injection into C57BL/6J mice (n=3 mice/group, 100 μg/mice).

D) The binding inhibition of PBAP-Her2 on PD-L1/PD-1 interaction was assessed by ELISA. The absorbance was measured at 450 nm to determine the blocking effect.

E) The fluorescence intensity of the antibody-cell binding was analyzed using a flow cytometer to assess the blocking effect on the PD-1/PD-L1 pathway.

F) Diagram illustrating the mechanism by which PBAP-Her2 synergizes with Trastuzumab and Kadcyla to kill PD-L1-positive target cells. Created with BioRender.com.

G) ADCC and ADCP activities were assessed using Jurkat-FcγR reporter systems: ADCC (FcγRIIIa-V158 variant) and ADCP (FcγRIIa-R131 variant) in response to PBAP-Her2/PBAP-gE combined with Trastuzumab. PBAP-Her2 in combination with Trastuzumab significantly enhanced ADCC and ADCP activities against Her2-negative MDA-MB-231 cells. Representative of 3 independent experiments.

H) NK cell-mediated cytotoxicity was quantified using an LDH release assay. The combination of PBAP-Her2 with Trastuzumab induced potent cytotoxicity against MDA-MB-231-PD-L1-OE cells, which was reduced following PD-L1 knockout in target cells (MDA-MB-231-PD-L1-KO). Representative of 3 independent experiments.

I) Flow cytometer analysis of IFN-γ expression and inhibitory receptor (NKG2A) levels in NK cells. Representative of 3 independent experiments.

J) The CCK8 assay was used to evaluate the cytotoxicity of commercial ADCs (Kadcyla and Adcetris) combined with PBAP-Her2. MDA-MB-231-PD-L1-OE cells were treated with PBAP-Her2 (10 μg/well) for 4 hours, followed by ADC drugs (Kadcyla or Adcetris) at various concentrations (0.1, 1, 10, 100, 1000 ng/ml). After 24 hours of incubation, cell viability was measured using the CCK8 assay. PBAP-Her2 with Adcetris and Her2 protein with Kadcyla were used as controls. Representative of 3 independent experiments.

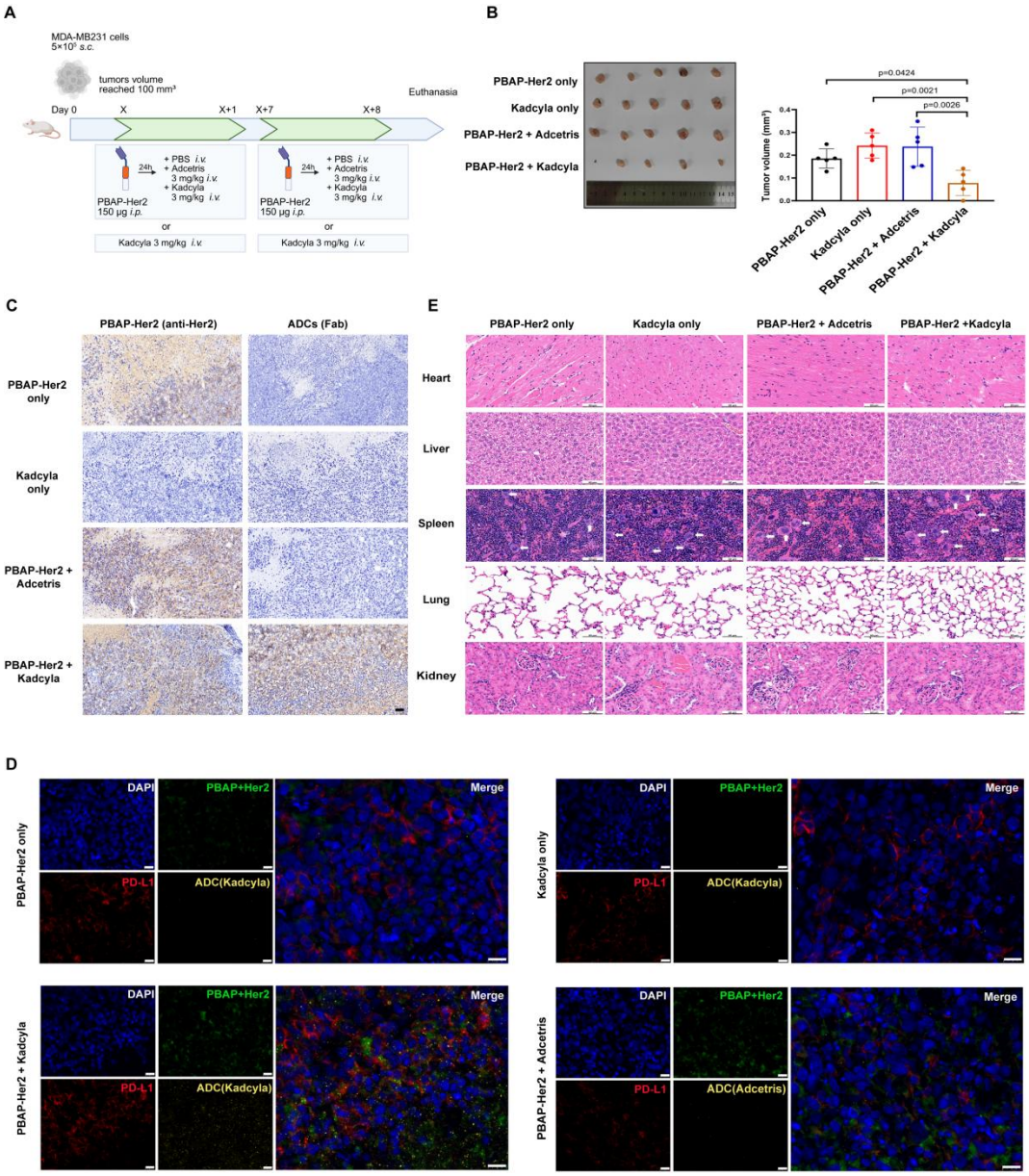

Fig. 7. PBAP-Her2 Synergizes with Antibody-Drug Conjugates to Enhance Antitumor Efficacy in NSG Mice Bearing Subcutaneous Tumors

A) Overview of Experimental Design. NSG mice were subcutaneously inoculated with MDA-MB-231 cells. Once the tumors reached approximately 100 mm^3, mice were assigned to one of four treatment groups (n=5 mice/group): PBAP-Her2 alone, Kadcyla alone, PBAP-Her2 + Adcetris, and PBAP-Her2 + Kadcyla. PBAP-Her2 (150 μg/mouse) was administered intraperitoneally, followed by tail vein injections of Kadcyla (3 mg/kg) or Adcetris (3 mg/kg) 24 hours later. Treatments were administered once a week for two consecutive cycles, with tumor growth monitored throughout the study. At the experimental endpoint, mice were euthanized, and tumor and tissue samples were collected for further analysis. Created with BioRender.com.

B) Representative tumor images for each experimental group are displayed on the left, with tumor volumes at the experimental endpoint shown in the right panel. Notably, the PBAP-Her2 + Kadcyla combination group demonstrated the most significant tumor regression, with clear tumor control, compared to other groups.

C) Immunohistochemistry (IHC) analysis was performed to assess the infiltration of PBAP-Her2 and ADC drugs into the tumors. The results showed that PBAP-Her2 effectively infiltrated the tumor tissue. Moreover, Kadcyla was found to infiltrate the tumor only when administered in combination with PBAP-Her2. In contrast, Adcetris failed to infiltrate the tumor in the PBAP-Her2 + Adcetris treatment group. Scale bars, 50 μm.

D) Immunofluorescence analysis further confirmed the specific efficacy of the PBAP-Her2 + Kadcyla combination. Tumor sections revealed clear co-localization of PBAP-Her2 with PD-L1 on tumor cells. Kadcyla was observed to enter tumor cells exclusively in the PBAP-Her2 + Kadcyla group. In contrast, no intracellular ADC uptake was detected in the control groups (PBAP-Her2 + Adcetris or Kadcyla only). Scale bars, 20 μm.

E) H&E staining showed no significant histopathological damage to major organs (heart, liver, spleen, lungs) in the experimental group, indicating a favorable safety profile. An increased presence of multinucleated giant cells was observed in the spleens, particularly in the PBAP-Her2 + Kadcyla group, as indicated by white arrows. Scale bars, 60 μm.

For panel B, data are presented as the mean ± s.d. Statistical significance was determined using one-way ANOVA.